2013

# Optical Waveguides and Structures for Short Haul Optical Communication Channels within Printed Circuit Boards

Nicholas J. Riegel
*Michigan Technological University*

# OPTICAL WAVEGUIDES AND STRUCTURES FOR SHORT HAUL OPTICAL COMMUNICATION CHANNELS WITHIN PRINTED CIRCUIT BOARDS

By

Nicholas J. Riegel

A DISSERTATION

Submitted in partial fulfillment of the requirements for the degree of

DOCTOR OF PHILOSOPHY

In Electrical Engineering

MICHIGAN TECHNOLOGICAL UNIVERSITY

2013

This dissertation has been approved in partial fulfillment of the requirements for the Degree of DOCTOR OF PHILOSOPHY in Electrical Engineering.

Department of Electrical and Computer Engineering

Dissertation Advisor: *Dr. Christopher Middlebrook*

Committee Member: *Dr. Paul Bergstrom*

Committee Member: *Dr. Craig Friedrich*

Committee Member: *Dr. Michael Roggemann*

Department Chair: *Dr. Daniel Fuhrmann*

# Contents

# List of Figures

# List of Tables

# Abstract

Optical waveguides have shown promising results for use within printed circuit boards. These optical waveguides have higher bandwidth than traditional copper transmission systems and are immune to electromagnetic interference. Design parameters for these optical waveguides are needed to ensure an optimal link budget. Modeling and simulation methods are used to determine the optimal design parameters needed in designing the waveguides. As a result, optical structures necessary for incorporating optical waveguides into printed circuit boards are designed and optimized.

Embedded siloxane polymer waveguides are investigated for their use in optical printed circuit boards. This material was chosen because it has low absorption, high temperature stability, and can be deposited using common processing techniques. Two sizes of waveguides are investigated, 50 $\mu$m multimode and 4 - 9 $\mu$m single mode waveguides.

A beam propagation method is developed for simulating the multimode and single mode waveguide parameters. The attenuation of simulated multimode waveguides are able to match the attenuation of fabricated waveguides with a root mean square error of 0.192 dB. Using the same process as the multimode waveguides, parameters needed to ensure a low link loss are found for single mode waveguides including maximum size, minimum cladding thickness, minimum waveguide separation, and minimum bend radius.

To couple light out-of-plane to a transmitter or receiver, a structure such as a vertical interconnect assembly (VIA) is required. For multimode waveguides the optimal placement of a total internal reflection mirror can be found without prior knowledge of the waveguide length. The optimal placement is found to be either 60 $\mu$m or 150 $\mu$m away from the end of the waveguide depending on which metric a designer wants to optimize the average output power, the output power variance, or the maximum possible power loss.

For single mode waveguides a volume grating coupler is designed to couple light from a silicon waveguide to a polymer single mode waveguide. A focusing grating coupler is compared to a

perpendicular grating coupler that is focused by a micro-molded lens. The focusing grating coupler had an optical loss of over -14 dB, while the grating coupler with a lens had an optical loss of -6.26 dB.

# 1 Introduction

In the late 1950's telecommunication engineers were looking for ways to increase the transmission bandwidth of current communication systems. AT&T had just launched their 300 bit per second modem and the big concern was how to transfer that much information over long distances. Two electric communication systems, the analog telephone and coaxial lines, were in heavy demand and the bandwidth was quickly being consumed. Transferring data using higher frequencies in the optical domain was hoped to be a solution to this problem, but the attenuation and lack of early optical fibers and a lock of an intense coherent source hindered progress. The invention of the laser in the 1960's, which could replace lossy broadband sources, caused fiber optics to be researched as a possible communication medium. For some time fiber optic communications stayed stagnant as the losses of fiber optic cables remained around 20 dB/km. Research remained stagnant until in 1964 when C. K. Kao and M. W. Jones determined that the fiber optic loss was due to impurities in the glass of the fiber optics[1]. Using better manufacturing standards to rid the glass of impurities Kao measured the bulk intrinsic loss of bulk fused silica as 4 dB/km and the fiber optic industry boomed [2]. Today fiber optic loss for long haul communications range from 0.15 dB/km to 0.40 dB/km, and optical fibers are the cheapest and most efficient way of transmitting data.

Several advantages of using fiber optics soon became apparent. The higher frequency of the optical fiber allowed for a greater bandwidth of the communication system. In the mid 1970's single mode waveguides were manufactured to lower the attenuation of the waveguides and increase the optical bandwidth. Since the different wavelengths of a single mode waveguide do not interfere with each other many parallel channels could be supported on one waveguide using coarse wavelength division multiplexing (CWDM) [3]. CWDM uses optical multiplexers which can be tailored to add or drop only one channel of light using optical gratings. This increases the bandwidth of the communication line by as many wavelengths that can be supported. By 1990 the wavelength spacing was decreased by dense wavelength division multiplexing (DWDM) was developed.

Another advantage of switching to optical waveguides was that they are not electrically conductive minimizing electromagnetic interference between two channels. Cross talk between two or more channels is reduced resulting in a lower bit error rate.

Increasing data rates on modern computers and computational systems have caused the bandwidth required to communicate chip to chip or board to board have increased exponentially in accordance with Moore's law [4]. Solving this problem requires the size of the electrical interconnects to become smaller so computational density can increase. As a result, copper interconnects have gotten to the nanoscale where the size of the trace is 32 nm [5]. Reducing the size of the electrical interconnect while increasing the bandwidth the high frequency losses dominate [6].

Printed circuit board manufactures are researching optical waveguides as a means of transmitting data for short haul communications[7, 8, 9, 10]. The hope when manufacturing optical waveguides is that optical waveguides can use the current processing techniques and industry standards set by the copper transmission lines. Manufacturing an optical printed circuit board (O-PCB), however, requires greater care in both design considerations and fabrication tolerances than those used in traditional copper transmission communication systems. An example of this difference is a copper trace can easily make a much tighter 90° bend, easing the routing of the copper transmission lines. Optical waveguide turns are required to have a minimum radius of curvature for constraining the light within the waveguide.

There are currently several short haul technologies emerging that may fill this need. Multimode waveguide technology is nearing the production phase of development [11]. The size of these multimode waveguides are usually in the range 30-100 $\mu m$. This technology has the drawback of a lower bandwidth compared to single mode waveguides because of modal dispersion. Each one of these modes travels at a different speed, therefore, faster data rates cannot be achieved because of intersymbol interference. Intersymbol interference also makes determining the exact output profile inconsistent making it more difficult to determine optimal coupling position. Multimode waveguides have the advantage of larger size. Making coupling into and out of the waveguide easier.

Another proposed short haul communication system under investigation utilizes single mode waveguides. These waveguides are smaller in size, typically around 4-10 $\mu$m, than the multimode waveguides making it harder to align and manufacture in a printed circuit board production line. The waveguide has one solution to the wave equation. This gives the single mode waveguide several advantages: it has a greater bandwidth since there is no intersymbol interference, it can support may channels using wavelength division multiplexing, and it has an easily determined output profile making it easier to determine the optimal coupling position.

A possibility for creating the mulitmode and single mode optical waveguides is using polymer siloxane waveguides. These materials can be manufactured using common processing techniques such as UV lithography, direct write, or direct dispense methods. They also have a low absorption coefficient which allows light to travel from the transmitter to the receiver with relatively little loss. Polymer waveguides exhibit high temperature stability which is needed for processing other components on a printed circuit board. The index of siloxane polymer waveguides are highly tunable to meet required manufacturing parameters such as index matching the waveguide to an optical fiber, minimizing coupling losses.

Implementing multimode and single mode waveguides into the printed circuit board process will require design rules, tolerances, and fabrication parameters to minimize the optical link budget. For example, as stated before, a waveguide cannot efficiently do an abrupt 90° in its propagation axis which is feasible with an electric transmission line [12]. To change the propagation axis of a waveguide, a large radius bend must be utilized to avoid appreciable radiation and coupling losses. When designing the waveguides it is also undesirable to make waveguides with arbitrarily large radius bends as that would greatly limit the feasible density of waveguides in the O-PCB layer. Accurate simulation will reduce the experimental cost in determining the manufacturing tolerances and design rules.

Optical vertical interconnect assemblies are required to couple light into and out of the embedded optical layer within PCB's with minimal loss. Since O-PCB's are made using planar methods, creating an out of plane bend would be a costly processing step. A different coupling method must be utilized. Two possible solutions to couple light out-of-plane from a source such as a vertical

cavity surface emitting laser (VSCEL) or a fiber to the waveguide layer are: using a lensed mirror and using a diffractive elements. A lensed mirror element is easier to design, manufacture, and more efficient in coupling the light, especially in the multimode waveguide case were each mode has a different effective index, but is harder to manufacture and align.

This dissertation addresses what design parameters need to be and how to couple the light out through modeling and simulation. Modeling and simulation methods are the most efficient means to determine these parameters without having to manufacture and test the waveguides, which may not be feasible. First it will explore the modeling methods used to simulate these components. Then, it will explore the effects of waveguide parameters such as bend radius attenuation, and sidewall roughness using the beam propagation method. These parameter are then confirmed by measuring the bend radius attenuation and sidewall roughness experimentally. The sidewall roughness and bend attenuation are then used to gain insight on what are the minimal parameters needed to minimize attenuation while maximizing waveguide packaging density on both multimode and single mode waveguides.

Next the dissertation designs and optimizes structures needed for short haul communication system. A total internal reflection mirror coupler is modeled for the optimal placement of a under filled highly multimodal waveguide. The optimal placement of the total internal reflection mirror will be found using without prior knowledge of the waveguide length itself, so the output waveform is not known. Finally, the dissertation will look at using a volume grating coupler to couple light from a silicon waveguide to a polymer single mode waveguide a compares using a focusing grating coupler to using a perpendicular grating coupler that is focused by a micro-molded lens.

Various waveguide parameters used in this dissertation are idealized, such as waveguide cross sectional shape. Different shapes of waveguides can vary the attenuation of the waveguide slightly. This dissertation focuses on the manufacturing parameters that are the most cost efficient to control or have the greatest effect on the waveguide performance. Actual attenuation of fabricated waveguides depends on the manufactures specific capabilities and may vary slightly from what is presented.

# 2 Simulation Models

There are two types of losses that occur when using optical waveguides: intrinsic losses and extrinsic losses. Intrinsic losses are due to scattering and absorption which are material dependent. These losses are not controllable through fabrication processes and can only be mediated by choice of material. Extrinsic losses such as coupling losses and waveguide sidewall roughness, are a result from fabrication and design processes. These losses can be minimized directly through the fabrication process. An accurate model is imperative to determine how fabrication methods will change the overall performance of the optical system. Several methods have been investigated to model the effects of short haul waveguides. Each method has distinct advantages and disadvantages which allow critical design parameters to be determined for the implementation of single mode and multimode waveguides embedded into printed circuit boards.

## 2.1 Ray Optics Model

Ray optics, or geometrical optics, is the easiest and least computationally intensive method to model a waveguide. The ray optics model is a simplified version of the wave optics model in which it is assumed that the wavelength of the light approaches zero, therefore does not have any diffraction effects [13]. This means light travels in a ray instead of a wave. This method is orders of magnitude faster than the other methods in which diffraction is accounted for and is an ideal method for modeling simple optical systems. It also provides users with an intuitive feel of which modes exist in the waveguide. This method fails, however, when calculating coupling coefficients between two waveguides (or different parts of the same waveguide) because it does not take into account phase matching conditions of the waveguide. Since this method does not take into account diffraction effects, this method cannot accurately model waveguide structures, such as waveguide bends and roughness.

Confining light within a waveguide is caused by having a core of a higher index of refraction ($n_0$) than the surrounding medium($n_1$), the cladding. This is shown in Figure 1. The rays are bound within the waveguide if the angle of the incident ray passes the critical angle given by:

$$\theta_c = \arccos(\frac{n_0}{n_1}) \tag{1}$$


Figure 1: Geometrical optics ray propagation.

There is an infinite number of angles that can satisfy the critical angle condition. To become a propagating mode the light must also constructively interfere or pass the self-consistency condition of:

$$(\frac{(\cos^2\theta - \sin^2\theta) * d}{\sin\theta} - \frac{d}{\sin\theta})n_0 k + 2\phi = 2m\pi, \quad m = 1, 2, \ldots \tag{2}$$

Where $d$ is the width of the waveguide, $k$ is the free space propagation constant of plane waves.

$$k = \frac{2\pi}{\lambda} \tag{3}$$

$\phi$ is the phase change caused by the $n_0$, $n_1$ boundary:

$$\phi = -2\arctan\left(\frac{\sqrt{n_1\, k\, \cos(\theta) - {n_2}^2\, k^2}}{\sqrt{n_1\, k\, \sin(\theta)}}\right) \tag{4}$$

For a wave that is polarized and has its electric field vector parallel to the interface and

$$\phi = n_1 \, k \, \cos(\theta) \tag{5}$$

for a wave that is polarized so its magnetic vector is parallel to the interface.

Finally, $m$ is an integer number corresponding to the mode number. Since the self consistency formulation can be satisfied when two waves are aligned in integer multiples of each other, several solutions of the equation exist if the width of the waveguide is high enough to allow more than one mode. These waveguides are called multimode waveguides.

The ray approach described above is the basis for finding the performance of a waveguide using geometrical optics. In the past this has been the preferred technique for modeling highly multimode waveguides because it is a simple approach that can run relatively quickly. However, since ray optics does not take into account diffraction and coupling effects, its modeling capability is limited. In short haul waveguides these modeling assumptions can not be used and a wave optics approach needs to be utilized.

## 2.2 Wave Optics Model

To achieve accurate coupling efficiencies, a wave optics model needs to be used. To model waveguides using wave optics, it is assumed that the waveguide is in a region with no charges, no currents, and is monochromatic. Therefore Maxwell's equations simplify to:

$$\nabla \cdot \vec{E} = 0 \tag{6}$$

$$\nabla \cdot \vec{B} = 0 \tag{7}$$

$$\nabla \times \vec{E} = -\frac{\partial \vec{B}}{\partial t} \tag{8}$$

$$\nabla \times \vec{B} = \mu_0 \varepsilon_0 \frac{\partial \vec{E}}{\partial t}. \tag{9}$$

Individual solutions to these equations form the modes of the waveguide. There are very few waveguide profiles in which the solutions to these equations are known, (slab waveguide, fiber waveguide). Analyses of other profiles need to be modeled using various assumptions. Depending on the assumptions used, different models emerge that solve this equation.

### 2.2.1 Finite Difference Time Domain

Maxwell's equations are able to be solved over a simulation domain if the index of the domain and the starting conditions of the simulation a known. This method solves Equation 8 and 9 explicitly over all the domain using time as the propagation variable. It separates each $E$ and $B$ component into its Cartesian coordinates ($E_x$,$E_y$...) for each computational unit cell known as the Yee cell, as shown in Figure 2 and relates the curl of the field to the time derivative. This method is known as the Finite Difference Time Domain method, or FDTD [14]. While solving for the specific field makes this method very robust, the model is very computationally intensive in both time and memory. The Yee cell size for FDTD simulations must be at least $\frac{\lambda}{2}$ so that Nyquist criteria is satisfied, which adds to computation complexity. The 2D model that has a reasonable size for modal mismatch coupling can have a least 660,000,000 elements that need to be calculated through 1,000,000 iterations. Using past run-times using the FDTD if can be found that this example will take approximately 360 hours to complete and use around 280 GB of memory. The 3D simulation will take 600 times as much memory and time. With the large computational time and memory requirements it is easy to see that finite difference time domain simulations should only be used for short distances. Instead of traveling 6 cm with the waveguide, traveling 1 mm will bring the memory requirements for a 2D simulation down to 5 GB and the time to 18 hours. 3D simulations run times are still too long for any reasonably short waveguide. Therefore, this method is the prime candidate to model small structures that have many reflections such as gratings couplers.

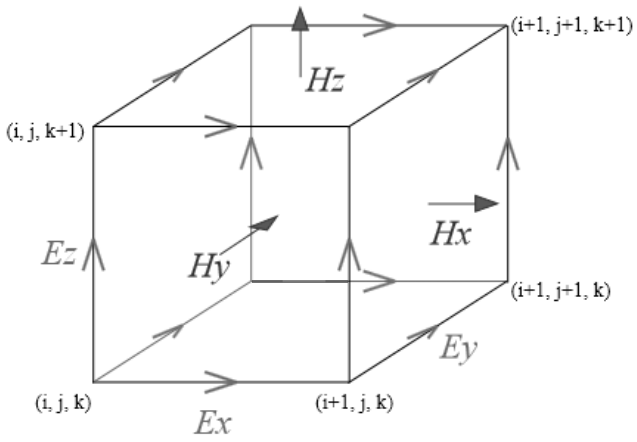


Figure 2: Finite difference time domain Yee cell.

### 2.2.2 Beam Propagation Method

Since the FDTD method is so computationally intensive, additional assumptions must be made to accurately model coupling in a waveguide. The Beam Propagation Method [15, 16] has been used as a solution to this problem. This method assumes that the wave evolves quickly in one direction compared to all other directions, the magnitude field changes slowly, and the solution is steady state. As such, this method is very quick in determining the steady state field in a straight waveguide (and a waveguide with bends using methods discussed later) and coupling coefficients between two waveguides or within the same waveguide.

The beam propagation method couples the Maxwells equations together to get one steady state equation. To couple the equations above the curl is taken on the Maxwell-Faraday equation and the Ampere's circuital law.

$$\nabla \times \nabla \times \vec{E} = -\frac{\partial}{\partial t}\nabla \times \vec{B} = -\mu_0 \varepsilon_0 \frac{\partial^2 \vec{E}}{\partial t^2} \tag{10}$$

$$\nabla \times \nabla \times \vec{B} = \mu_0 \varepsilon_0 \frac{\partial}{\partial t}\nabla \times \vec{E} = -\mu_o \varepsilon_o \frac{\partial^2 \vec{B}}{\partial t^2} \tag{11}$$

By using the vector identity:

$$\nabla \times \left(\nabla \times \vec{V}\right) = \nabla \left(\nabla \cdot \vec{V}\right) - \nabla^2 \vec{V} \tag{12}$$

The wave equation is formed:

$$\left(\nabla^2 - \mu\epsilon \frac{\partial^2}{\partial t^2}\right) \vec{E} = 0 \tag{13}$$

$$\left(\nabla^2 - \mu\epsilon \frac{\partial^2}{\partial t^2}\right) \vec{B} = 0 \tag{14}$$

If $\vec{E}(r,t)$ and $\vec{B}(r,t)$ are separable such that:

$$u(r,t) = A(r)T(t) \tag{15}$$

Where A is the amplitude of the wave and T is the time dependence. The wave equation may be simplified further to:

$$\frac{\nabla^2 A}{A} - \frac{\mu\epsilon}{T}\frac{d^2T}{dt^2} = 0 \tag{16}$$

Using the identity:

$$-\frac{\mu\epsilon}{T}\frac{d^2T}{dt^2} = k^2 \tag{17}$$

Where $k$ is the wavenumber. You get the commonly known Helmholtz equation

$$\nabla^2 A + k^2 A = 0 \tag{18}$$

Assuming A is a plane wave of the form:

$$A(x, y, z) = a(x, y, z) \exp^{i\beta z} \tag{19}$$

Separating the variables a finite difference equation of is produced:

$$\frac{\partial a}{\partial z} = \frac{i}{2\beta}(\frac{\partial^2 a}{\partial x^2} + \frac{\partial^2 a}{\partial x^2} + (k^2 - \beta^2)a) \tag{20}$$

This equation can be solved through evolving each plane in $z$ based on the previous plane using finite difference methods. For a given input of $a(x, y, z = 0)$ the model is able to solve all other $z$ planes. This method is very fast because the number of points that are needed to calculate for each iteration is minimal. The number of iterations can also be minimized by a coarse $z$ direction step size which can be run because time dependence does not need to be sampled. For example, a normal 50 $\mu$m width, 6 cm long, multimode waveguide, a 2D simulation will have 1,100 points that need to be calculated for each $z$ step and have about 60,000 iterations. This simulation takes about a minute. When the simulation is brought to a 3D simulation there will be 1,210,000 points that need to be calculated for each $z$ step and it will still have about 60,000 iterations. This simulation takes considerably longer, about 36 hours.

Although the beam propagation method is the least memory constricting and runs the fastest under non-ideal conditions, several disadvantages result because of the assumptions made. It

was assumed the wave has the form of a plane wave the model with a slow changing field and is inaccurate when modeling a fast changing field. With the assumption that the field was separable, only the steady state solutions can be solved. Therefore, waveguide characteristics such as dispersion cannot be solved. In addition, the field can only propagate in the $z$-direction. A consequence of this error is shown in Figure 3 were in which a field along a 45° direction from the $z$-axis was propagated.

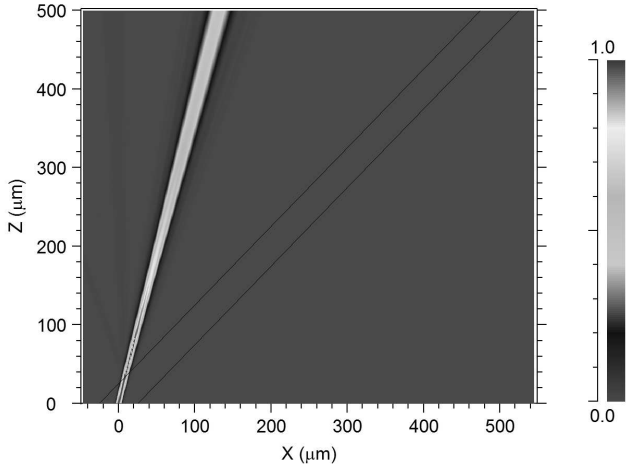


Figure 3: Limitations in propagating field in the $x$ direction using beam propagation method.

### 2.2.3 Coupled Mode Theory

Another way to model waveguides is using coupled mode theory. This method uses the known solutions or approximations of the Maxwell's Equations to propagate down a waveguide with the modes effective index. Coupled mode theory works because each mode in a waveguide is orthogonal to all other modes so that Equation 21 is realized.

$$\int\int \vec{E}_m(x,y)\vec{E}_n(x,y)\,dxdy = 0, \quad \forall\ m \neq n \tag{21}$$

This means that each input field may be written as:

$$\vec{E_i}(x,y) = \sum_{m=0}^{M} \left( a_m \vec{E}_m(x,y) \right) + loss \tag{22}$$

Using the orthogonality principle $a_m$ can be rewritten as:

$$a_m = \int \int \vec{E_i}(x,y) \vec{E}_m(x,y)\, dxdy, \quad \forall\ a_m \tag{23}$$

Plugging each $a_m$ into Equation 22, the loss associated due to modal mismatch can be found.

Example solved modes for a waveguide are shown in Figure 4. Each of these modes travel at a different speed, $\beta$. Using this knowledge the modal dispersion of the waveguide can be determined. This method is considerably more accurate in fast changing conditions than the beam propagation method. This method of modeling also runs very fast if the waveguide profile is not changing or if the waveguide profile is mathematically known, such as in the case of a slab waveguide and a cylindrical fiber. The number of modes in a highly multimodal square waveguide may be approximated as:

$$N_{Modes} \approx \pi\, NA^2 (\frac{d}{\lambda}) \tag{24}$$

Where $d$ is the width of the waveguide and $NA$ is the numerical aperture given by

$$NA = \sqrt{n_{core}^2 - n_{clad}^2} \tag{25}$$

When the waveguide modes are not known, or the number of modes that are needed to be calculated is very large, this method falls apart because the computational time needed to compute all the possible modes that the waveguide can support.

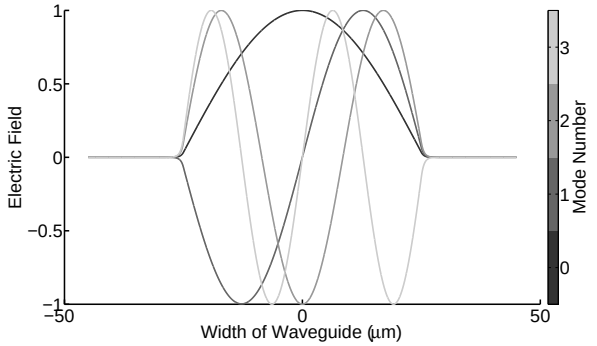


Figure 4: Modal solutions for a slab waveguide.

### 2.2.4 Angular Spectrum

If a field propagates in a uniform media, such as free space, the field may be decomposed to a superposition of plane waves across an input pupil. A plane wave can be written as:

$$A\, e^{j(\vec{k}\bullet\vec{r})} \tag{26}$$

Where $\vec{k}$ is the wave vector and $\vec{r}$ is the direction of the plane wave. such that:

$$\vec{k} = \frac{2\pi}{\lambda}\left(\alpha\hat{x} + \beta\hat{y} + \gamma\hat{z}\right) \tag{27}$$

and

$$\vec{r} = x\hat{x} + y\hat{y} + z\hat{z} \tag{28}$$

Decomposing the input field into a continuum of plane waves at the pupil can then be written as a Fourier transform of the pupil as:

$$U(\frac{\alpha}{\lambda}, \frac{\beta}{\lambda}, 0) = \iint_{-\infty}^{+\infty} a(x, y, 0)\, e^{-j\,\frac{2\pi}{\lambda}(\alpha x + \beta y)}\, dx\, dy \tag{29}$$

The field is propagated by:

$$U(\frac{\alpha}{\lambda}, \frac{\beta}{\lambda}, z) = U(\frac{\alpha}{\lambda}, \frac{\beta}{\lambda}, 0)\, e^{j\,\frac{2\pi}{\lambda}\sqrt{1-\alpha^2-\beta^2}z} \tag{30}$$

The resultant field can then be reconstructed using an inverse Fourier transform:

$$u(x, y, z) = \iint_{-\infty}^{+\infty} U(\frac{\alpha}{\lambda}, \frac{\beta}{\lambda}, z)\, e^{j\,\frac{2\pi}{\lambda}(\alpha x + \beta y)}\, d\frac{\alpha}{\lambda}\, d\frac{\beta}{\lambda} \tag{31}$$

This method assumes that the medium is constant throughout the propagation and solves the Helmholtz equation explicitly, therefore it is a very accurate and fast way to model an input field. The problem arises because the input and output field must be sampled at [17]:

$$N_{x,y} = \frac{2\lambda z}{dx^2} \tag{32}$$

This makes it difficult to model fields propagating over a great distance compared to the sample spacing, as the required samples approach an very large number. If a waveguide is sampled at 0.01 $\mu$m and the wavelength is 1310 nm, propagating 1 mm would require a $2.62 * 10^7$ x $2.62 * 10^7$ matrix. As such, the angular spectrum is only used in the near field of the pupil.

# 3 In-Plane Performance of Mulimode Wavegudies

The Shannon-Hartley theorem is one of the most powerful equations in information theory because it calculates maximum rate at which information can be transmitted over a communications channel. Using this theory the maximum rate of information that can be transmitted over a channel can be calculated by

$$C = B \log_2(1 + \frac{S_r}{N}). \tag{33}$$

Where $C$ is the channel capacity, $C$ , $B$ is the bandwidth, $S_r$ is the received signal power, and $N$ is the system noise. Decreasing $N$ in this equation is costly, as it usually requires expensive cooling of the transmitter and receiver. As such, it is normally used only in long haul communication systems. The bandwidth of a short haul communication system is limited by the transmitters or the detectors of the system and is not usually a design issue because of the short communication length. Therefore, the best way to increase the channel capacity is to increase the received power, $S_r$. The received signal power can be broken down to:

$$S_r = S_{in} - S_{loss} \tag{34}$$

To increase the received power a designer can increase the input power, $S_{in}$, but this comes at the cost of higher power needed for the communication link. This method experiences diminishing returns as a raise in input power, $S_{in}$, also increases the noise of the system, $N$. The best way to increase the channel capacity is to lower the loss of the system $S_{loss}$.

$S_{loss}$ is a function of the distance of the waveguide and is characterized by:

$$S_{loss} = S_{in}\, e^{-\alpha_m * L} + S_{insertion} \tag{35}$$

Where $S_{insertion}$ is the coupling loss of the waveguide and $\alpha_m$ is the constant loss which can be broken down to

$$\alpha_m = \alpha_{material} + \alpha_{scattering} + \alpha_{radiative} \tag{36}$$

Where $\alpha_{material}$ is the absorption of the material, $\alpha_{scattering}$ is the loss because of manufacturing processes such a roughness, and $\alpha_{radiative}$ is the loss due to the geometry of the waveguide such as a small radius bends. When the light is confined in a perfect waveguide ($\alpha_{fabrication} = 0$) the loss of the waveguide systems is very low, around the intrinsic loss of the waveguide material, on the order of 0.01 dB/cm. A perfect waveguide system, however, is not realizable and not applicable for mass manufacturing of waveguides as it would be cost prohibitive. Previous research has shown that the material losses are not the underlying factor in overall waveguide attenuation [18]. Therefore, ensuring an accurate model of scattering and radiative losses in a waveguide is paramount to determining the attenuation of a waveguide. An accurate model of the radiative losses demonstrates the minimum radius bend a waveguide can have. An accurate model of the scattering losses helps show the performance gains by making the material less rough. Several methods have been proposed to minimize roughness losses in polymer waveguides including finer lithographic mask resolution [19], thermal-reflow technique [20], and micro-molding [21].

The multimode waveguides used are lithographically defined as 50 $\mu$m x 50 $\mu$m channels of a waveguide. This waveguide size is used because it easily couples to a standard 50/125 $\mu$m (50 $\mu$m circular core with 125 $\mu$m cladding) multimode fiber. The materials used were Dow Corning's ©OE 4140 for the cladding and OE 4141 for the core. A wavelength of 850 nm was used for the optical communication. This wavelength was chosen because the energy in a photon of light, as shown in Equation 37, is larger than the band gap of silicon of 1.11 eV [22], therefore inexpensive detectors can be made and are easily fabricated into existing Silicon manufacturing processes.

$$E = \frac{h\,c}{\lambda} \tag{37}$$

The cladding index of the material is 1.50 and the core index of the material is 1.52. The numerical aperture (NA), given by Equation 25, of the waveguide using the cladding and core refractive indexes is 0.246.

Several attempts to characterize the effects of roughness on highly multimodal waveguides have been made using coupled mode theory or Fourier decomposition method [23, 24, 25, 26, 27]. Coupled mode theory, however, is not easily adaptable to structures such as waveguides containing short radius (410 mm) bends. While the modal distribution of waveguides with bends are defined mathematically [28] for the 2D case, the high order Bessel functions to be solved with formulations, such as coupled mode theory, are out of range of current numerical libraries [29], therefore making them inaccurate or too time consuming to evaluate. These limitations can be alleviated by matching power performance of waveguides modeled by the beam propagation method (BPM) [15, 16] to waveguides fabricated in the lab for both straight and bent waveguides.

## 3.1 Measurement of Fabricated Waveguides

To measure the attenuation of the fabricated waveguides the cutback method [30] was used. Use of the cutback method determines the waveguide loss per distance and the insertion loss by measuring the loss of the waveguide at a larger distance, then cutting back the waveguide to a shorter distance and repeating this step multiple times. The attenuation in the waveguides is a exponential curve (or linear curve in dB scale) depending on the length of the waveguide. The slope of the resulting curve corresponds to the constant loss, $\alpha_m$, while the y-intercept corresponds to the insertion loss, $S_{insertion}$.

To measure the attenuation of the waveguide, a 5.6 $\mu$m with a NA of 0.124 single mode fiber was used to illuminate the fabricated waveguide with 2 mW of light at $\lambda = 830$ nm. The fiber was placed at the center of the waveguide to only excite the even modes of the waveguide. The position of the fiber was desirable since this most closely matches the attenuation suffered in a mass fabricated optical printed circuit board (O-PCB) setup. The fiber size was desirable because it is a single mode waveguide, so the input waveform is the same for each time the waveguide

is measured. The guided light was then captured with a 50 $\mu$m multimode fiber, with an NA of 0.201 and measured with a silicon detector. The difference in NA between the waveguide and the multimode fiber causes the highest order modes not to be coupled. Even with the higher order modes not coupling the results should be consistent with the true attenuation because of the nature of the cutback method and the comparatively low amount of power in the higher order modes compared to the lower order modes. Index matching fluid was utilized to lessen the insertion losses between optical fibers and the waveguide.

A set of four waveguides were fabricated with varying lengths. The length of the first set of waveguides was 6.76 cm. The power loss was recorded for each channel on four separate occasions then averaged. The guides were then milled to 4.84 cm then remeasured four times for each channel. This process continued for waveguides of length 3.81 cm and 1.91 cm. The results using the cutback method are shown in Figure 5 by the slope of the regression line the attenuation was determined to be 0.045 dB/cm with an insertion loss of 0.073 dB. This fit had a coefficient of determination ($R^2$) of 0.8293. Several outliers show up in Figure 5, especially at 3.805 cm length and 4.839 cm. The differences between the measured intensities and the attenuation line is less than 1.5% of the received power. This is attributed to differences in the cut quality of the waveguide endface.

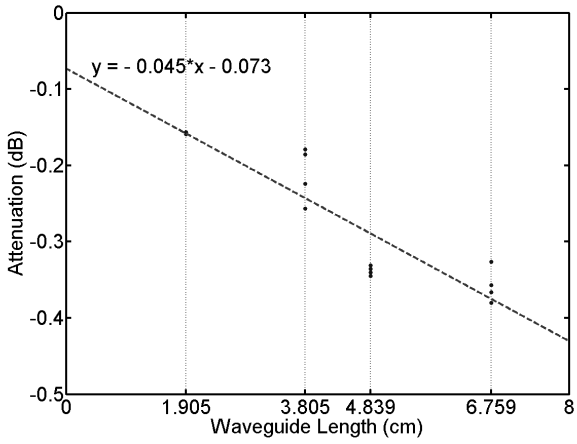


Figure 5: Cutback method losses in straight waveguide.

## 3.2 Straight Waveguides Simulation

The parameters used in the simulation are shown in Table 1. The beam propagation simulation was preformed using BeamProp, which is the beam propagation method module under the RSoft$^{TM}$Photonics CAD Suite. The simulation consisted of three lateral regions: the waveguide core region, the cladding region, and a boundary absorbing region as shown in Figure 6. The core and the cladding region were consistent with the index and the size of the fabricated waveguides, while the absorption region was added to reduce the amount of power reflection on the simulation boundaries. The simulation used simple transparent boundary conditions [31]. These boundary conditions are the most suitable for highly multimodal problems in BeamProp [32]. Sampling conditions were found by a convergence study using a 2D BPM effective index simulation and are shown in Table 1. Using these sampling conditions, the power output of a 4 mm radius turn varied by no more than 1%. The input waveform of the straight simulation was chosen to be a 5.6 $\mu$m single mode fiber operating at a wavelength of 850 nm. The simulation was run using only the foreword scattering model because backscattering in this case is minimal, ($10^{-10}$ dB), at the roughness and correlation lengths used in the simulation.

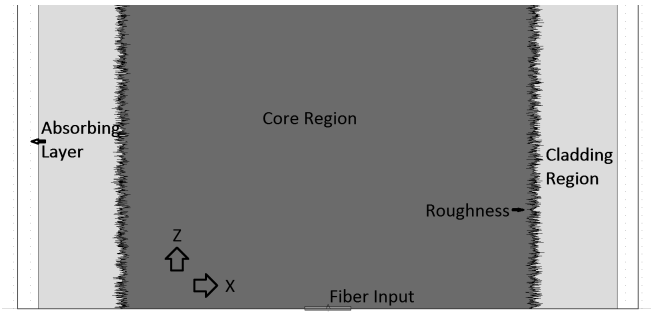


Figure 6: Simulation regions.

### 3.2.1 Waveguide Roughness

Roughness on a waveguide, which is shown in Figure 7, can be modeled as a slight deviation from the original waveguide such that the waveguide's width and the center of the waveguide are

Table 1: Beam propagation method simulation parameters.

| Parameter | Value |
|---|---|
| Wavelength | 850 nm |
| Input Fiber Diameter | 5.6 $\mu$m |
| Input Fiber NA | 0.24 |
| Real Index Core | 1.52 |
| Real Index Clad | 1.50 |
| Absorption Clad/Core | 0.01 dB/cm |
| Absorption Region Absorption | 1 dB/cm |
| Waveguide Width | 50 $\mu$m |
| Sample Size $\Delta x$,$\Delta y$ | 0.02 $\mu$m |
| Sample Size $\Delta z$ | 1 $\mu$m |
| Normal Cladding Region | 20 $\mu$m |
| Absorbing Cladding Regoin | 10 $\mu$m |
| Boundary Conditions | Simple Transparent Boundary Conditions |
| Padé order | (1,1) |

slightly offset by random functions:

$$w(z) = w_0(z) + \Delta w_{x,y}(z) \tag{38}$$

$$M(z) = M_0(z) + \Delta M_{x,y}(z) \tag{39}$$

Where $w_0$ and $M_0$ is the width geometric center of the unperturbed waveguide and $\Delta w$, $\Delta M$ are the deviations from the ideal waveguide. Waveguides that are lithographically defined tend to have the greatest roughness along the sidewall so that the roughness of the waveguide is predominately in the y-z plane which is shown in Figure 7. Therefore, the roughness in the x-z plane can be neglected. Simplifying Equations 38 and 39 to the following:

$$w(z) = w_0(z) + \Delta w_{yz}(z) \tag{40}$$

$$M(z) = M_0(z) + \Delta M_{yz}(z) \tag{41}$$

The validity of this assumption was proven by observing the roughness profile with a field emission scanning electron microscope (FE-SEM) as shown in Figure 8 and measuring the roughness

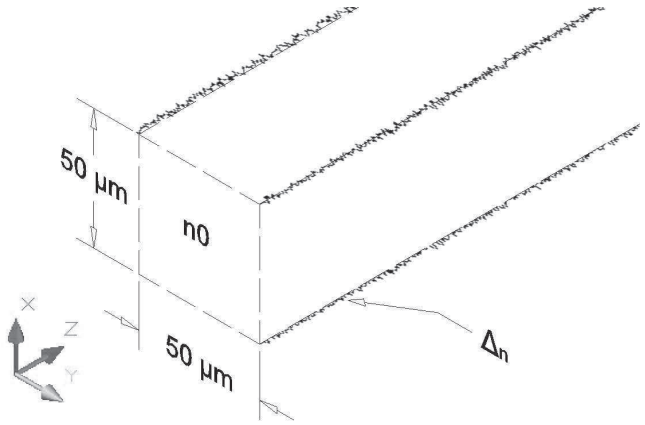


Figure 7: 3D Beam propagation setup for sidewall roughness.

with an infinite focus microscope which is shown later in Section 3.1. The sidewall roughness was at least five times greater than the roughness at the top of the waveguide, the sidewall roughness was shown to have an RMS of 46 nm while the top roughness had an RMS of 7 nm. Furthermore, it was assumed that the roughness of the waveguide had a wide sense stationary noise with autocorrelation of the roughness characterized by the commonly used exponential function [33, 34]:

$$C_w(z) = \Delta w_y e^{-\frac{|z|}{L_c}} \tag{42}$$

$$C_M(z) = \Delta M_y e^{-\frac{|z|}{L_c}} \tag{43}$$

Where $L_c$ is the autocorrelation of the roughness and $z$ is the length along the waveguide.

### 3.2.2 Sampling Constraints

The beam propagation method sampling of the sidewall roughness was preformed using either a non-uniform mesh or a course mesh with a linear interpolation function to reduce computational time. The non-uniform mesh first samples the inside of the waveguide with a coarse mesh then on the edges of the waveguide the mesh gets smaller to incorporate the effects of sidewall roughness. This method alleviates the need for fine sampling across the entire waveguide, but still takes more

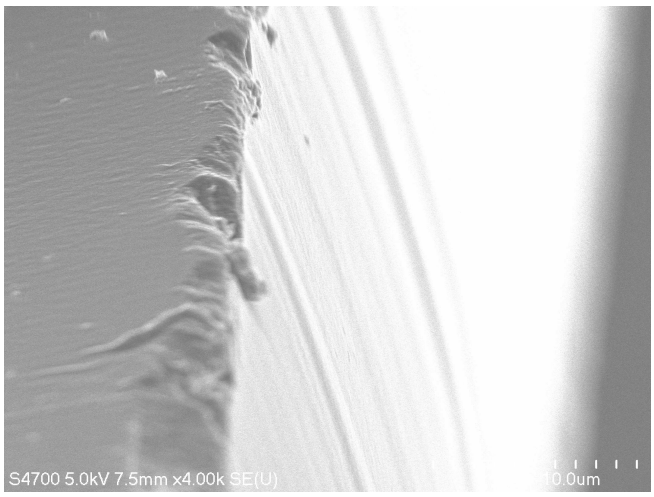


Figure 8: Edge view of waveguide sidewall roughness of a 25 $\mu$m x 50 $\mu$m straight waveguide found using Hitachi S4700 FE-SEM.

time than coarse sampled waveguide. The other option is to use an interpolation function across the sample area to generate an average index between two sample points. Using this method it is possible to simulate the effects of lithographic roughness without increasing runtime, as long as the sample size of the simulation remains under the critical sampling condition. Figure 9 shows the difference between the output attenuation, in dB, of a non-uniform mesh straight waveguide simulation with 50 $\mu$m roughness with the boundaries sampled at 0.1 nm and a uniform coarse mesh simulation. This shows that if the sample size of the waveguide remains under 0.04 $\mu$m the attenuation of a straight waveguide varies by less than 0.4 %.

### 3.2.3 2D vs 3D Model Considerations

A single run of the beam propagation method is shown in Figure 10. On the right hand side the evolving electric field amplitude as the beam propagates down the length of the waveguide is shown. As the beam propagates down the length of the waveguide, each mode constructively and destructively interferes with each other creating a different electric field distribution for each length. The amount of power is contained in the waveguide plus about 2.5 $\mu$m on the outside of the waveguide to account for the evanescent fields of each mode is shown on the right.

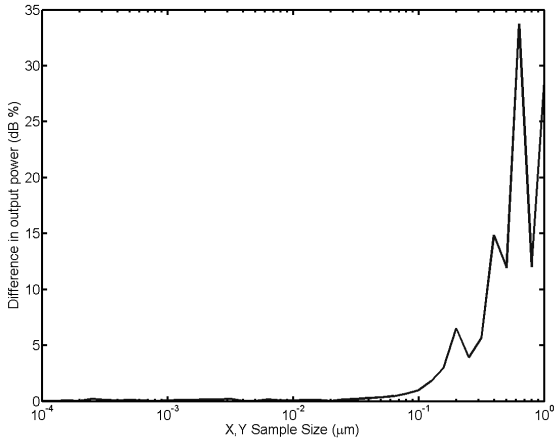


Figure 9: Attenuation sample size error of a straight waveguide with a roughness of 50 nm RMS and a correlation length of 3 $\mu$m.

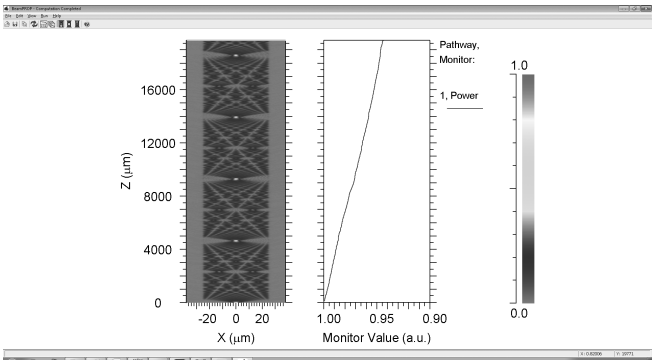


Figure 10: A single run of the 2D beam propagation method.

By changing a parameter in the simulation, such as the roughness strength of the waveguide, a distribution of attenuation may be made from the resulting graphs. Fitting the measured attenuation of the waveguides to the simulated attenuation, an estimate of the roughness can be estimated. For example, in Figure 11 if the slopes of the attenuation after the modal coupling losses which show up in the first 0.1 cm propagation are matched, an estimate of the roughness in the waveguide can be found.

Until now, in this dissertation, the beam propagation method results have only been shown in a 2D beam propagation simulation. The 2D simulation assumes that the waveguide is infinite in the y-direction. While this assumption is not accurate, the simulation times for these simulation are

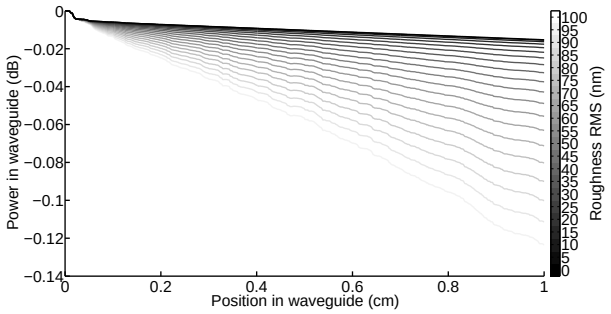


Figure 11: Changing the roughness in the 2D beam propagation method.

much less than 3D simulation elapsing about a half minute up to three minutes. 3D simulations take many times longer, usually lasting about three to twelve hours. One way to lessen the burden of this assumption is to use the effective index method [35]. Unfortunately, for the $\mu$m waveguide used this requires 266 different 2D simulations which approach the time of the 3D simulation. Figure 12 shows how sidewall roughness effects waveguide attenuation depending on the method used. The attenuation found in the fabricated waveguides is matched the roughness that was found using the 3D BPM, 2D BPM, and effective index method was 60.2 $\mu$m, 63.4 $\mu$m, 62.8 $\mu$m respectively. Based on results, it was determined that the 3D beam propagation method simulations were needed for accurate modeling of the waveguides.

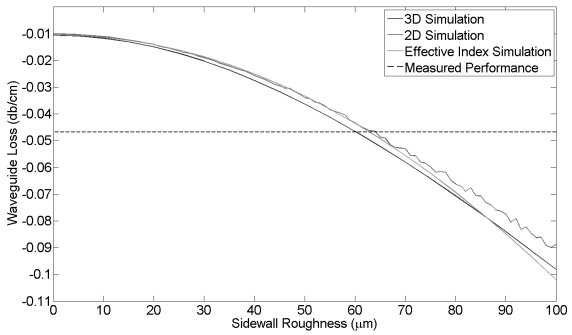


Figure 12: Comparison of beam propagation methods.

### 3.2.4 Physical Verification of Roughness

To verify the roughness result from the straight simulation, the sidewall roughness of the experimental waveguides was measured using interferometric microscopy (IFM). IFM uses an interference pattern of white light to determine the roughness of a sample. The machine used, the Phase Shift MicroXAM, can sample depth with a resolution of 0.5 nm and a lateral resolution of 0.22 $\mu$m [36]. The roughness at the top of the waveguide was measured to be 6 nm and it had very little correlation between the roughness samples, therefore the effect of this roughness was ignored. The sidewall roughness was measured by dispensing Dow Corning's ©OE-4140 core material onto a glass substrate. Using a lithographic mask that had a resolution of 0.5 nm, therefore it can be assumed that the roughness on the side of the waveguide is roughly the same as on the waveguide bends. Waveguides were then diced using a dicing saw about 2 $\mu$m from the waveguide. The diced components were then cleaned with compressed air to remove any particles left from the dicing saw. Holding the waveguide on its side, the sidewall roughness could be measured. The roughness, shown in Figure 13a, resulted in a root mean square (RMS) roughness of 46 nm with a long correlation length of $L_c = 3$ $\mu$m as shown in Figure 13b. This value is much higher correlation length then other researchers have reported [23, 24, 25]. This difference may be attributed to the masks used for the lithographic pattering, differences in the polymer material for the waveguide, or low spatial frequency effects [37].

## 3.3 Simulation of Waveguides with 90° Turns

### 3.3.1 Coordinate Transformation for Simulation

As explained in Section 2.2.2, the beam propagation method cannot accurately model waves that travel beyond 1 or 2° in the $x$ or $y$ direction. Modeling a bend using the beam propagation method is inaccurate in the later part of the curve. To overcome this limitation a conformal transformation is utilized [38]. This transformation, shown in Equation 44, transforms the Z plane shown in Figure 14b to the W plane shown in Figure 14a. This transform is made possible by changing the index of the system, $n(x, z)$ to $n_{eff}(u, v)$.

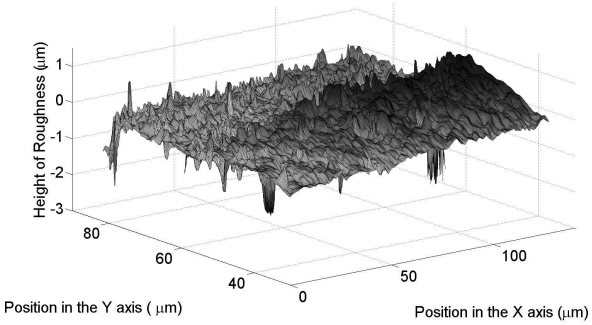


(a) Roughness profile found with the IFM.

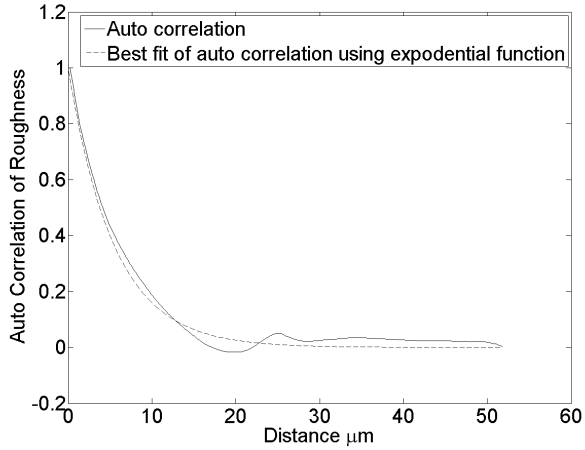


(b) Autocorrelation of the measured roughness along the direction of light propagation.

Figure 13: Waveguide sidewall roughness measured using the Phase Shift MicroXAM IFM.

$$W = u + jv = R \ln\left(\frac{Z+R}{R}\right) \tag{44}$$

Where

$$Z = x + jz \tag{45}$$

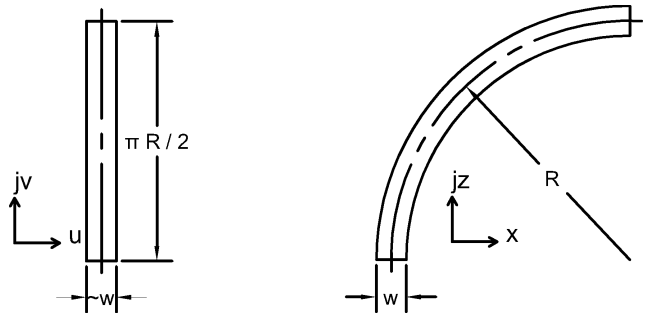


(a) Waveguide bend profile after conformal transformation.

(b) Waveguide bend profile before conformal transformation.

Figure 14: Coordinate transformation of a curved waveguide to straight waveguide using conformal transformations.

Separating the transformation into the components of the W plane

$$u = R \ln \left( \frac{\sqrt{(x+R)^2 + z^2}}{R} \right) \tag{46}$$

$$v = R \tan^{-1} \left( \frac{z}{x+R} \right) \tag{47}$$

Which satisfy the the Cauchy Riemann relations of

$$\frac{\partial u}{\partial x} = \frac{\partial v}{\partial z} \tag{48}$$

$$\frac{\partial v}{\partial x} = -\frac{\partial u}{\partial z} \tag{49}$$

Using the transformation

$$\nabla^2_{x,z} = \left( \left( \frac{\partial u}{\partial x} \right)^2 + \left( \frac{\partial v}{\partial x} \right)^2 \right) \nabla^2_{u,v} \tag{50}$$

and substituting it into the Helmholtz equation, the effective index of the transformed waveguide is found as

$$n_{eff}(u,v) = e^{\frac{u}{R}} n\left(x(u,v), z(u,v)\right) \tag{51}$$

Here it was approximated that when $z = 0$

$$u = R \ln\left(\frac{x+R}{R}\right) \approx x - \frac{x^2}{2R} \tag{52}$$

There is a slight transverse component when changing coordinates from the straight to curved waveguides. Given that Equations 53 and 54 hold true, the width, the roughness size, and statistics using the conformal transformation remains unchanged as seen in Equations 55 and 56.

$$\sigma^2 \ll R \tag{53}$$

$$w\sigma \ll R \tag{54}$$

$$\hat{w} = u\left[\frac{w}{2}\right] - u\left[\frac{-w}{2}\right] = w \tag{55}$$

$$\hat{\sigma} = u\left[\frac{w}{2}\right] - u\left[\frac{w}{2} - \sigma\right] = \sigma^2 - \frac{w\sigma}{R} - \frac{\sigma^2}{R} \approx \sigma \tag{56}$$

### 3.3.2 Bends Simulation Correlation to Experimental Results

The simulation consisted of three lateral regions: the waveguide core region, the cladding region, and a boundary absorbing region. Additionally included were three sectors along the $z$-direction of a radius length straight, the quarter bend, and another radius length straight as shown in Figure 15.

The waveguides with bends were measured using the same light coupling methods used in the straight waveguides as discussed in Section 3.1. The bends of the lithography-based sample's bends ranged from 1 to 10 mm radii in increments of 1 mm where each radii had 8 sets of waveguides. They consisted of a straight section that is the curvature radius in length followed by a quarter turn of the radius followed by another straight of 1 cm plus the radius of the bend in length. This geometry was necessary to fit all the radii on a single board layer. Utilizing the previously calculated values of insertion loss of 0.073 dB found in Section 3.1, the losses for the waveguides including bends were determined. Two different sets of simulations were performed.

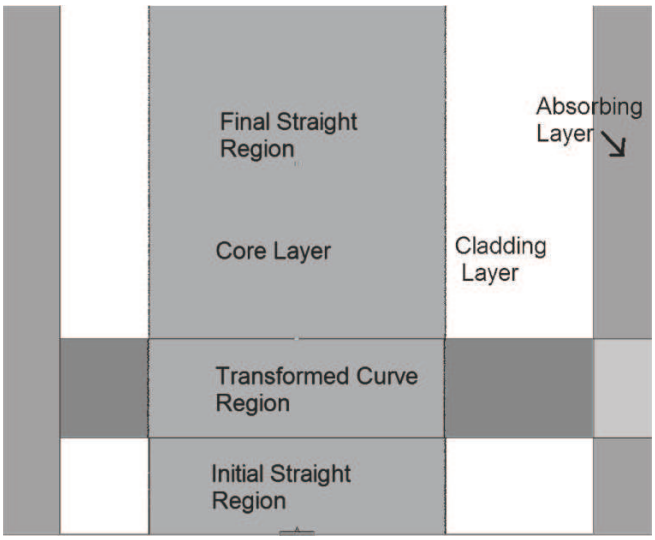


Figure 15: Beam propagation method model used for simulation of waveguides with 90° bends.

Both sets of simulations used the same parameters previously found in Table 1, except the $\Delta x$ and $\Delta y$ were shortened to 0.005 $\mu$m for one simulation and 0.010 $\mu$m for the other to ensure stability. The results of the simulation with 0.005 $\mu$m spacing and the measured fabricated attenuation are shown in Figure 16.

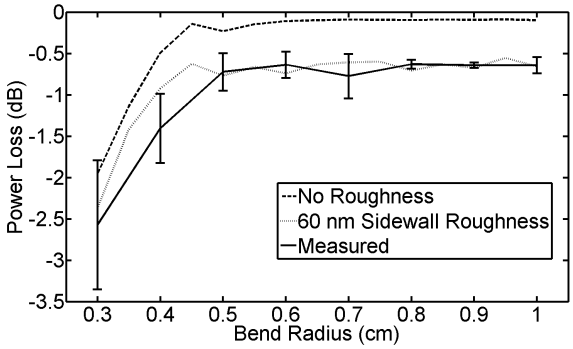


Figure 16: Comparison of simulated and measured bends.

The correlation coefficient (CC) and the mean square error (MSE) of the attenuation based on the radius of the bends between the measured and the simulated results are shown in Table 2. The coefficients were found by averaging the attenuation for 8 fabricated sets of waveguides for each radii then comparing the simulated data to the fabricated. The simulations show that the correlation coefficient of the waveguide with no roughness is a better match than the correlation

coefficient of the rough waveguide. This can be due to averaging the attenuation of each radii, giving a smoother curve. To overcome the limitation on the rough waveguide, several runs could be performed in order to provide a more representative averaged smooth curve. However, additional runs were not conducted. One simulation took 17 days to run. This is justified because mean square error was greatly reduced by adding the roughness to the simulation. The attenuation difference between the 0.005 $\mu$m simulations and the 0.010 $\mu$m simulations differed by less than 1%, therefore the simulation was considered stable.

Table 2: Figures of merit.

| Parameter | Sample Spacing | Roughness | Value |
|---|---|---|---|
| CC | 0.005 $\mu$m | 60 nm | 0.9633 |
| CC | 0.005 $\mu$m | none | 0.9810 |
| CC | 0.010 $\mu$m | 60 nm | 0.9591 |
| CC | 0.010 $\mu$m | none | 0.9783 |
| | | | |
| MSE | 0.005 $\mu$m | 60 nm | 0.0370 $\mu$m$^2$ |
| MSE | 0.005 $\mu$m | none | 0.2442 $\mu$m$^2$ |
| MSE | 0.010 $\mu$m | 60 nm | 0.0520 $\mu$m$^2$ |
| MSE | 0.010 $\mu$m | none | 0.1815 $\mu$m$^2$ |

## 3.4 Conclusion

Manufacturing parameters for multimode waveguides for use in optical printed circuit boards were found using the beam propagation method. To find the optimal parameters, straight multimode waveguides were fabricated using Dow Corning's ©OE-414x material. Using the cutback method, the attenuation of the straight waveguides was determined to be 0.045 dB/cm with a insertion loss of 0.073 dB. The attenuation found using the cutback method was used to determine the sidewall roughness of a waveguide using simulations. The roughness was found to be, $\sigma = 60$ nm using the simulations. The roughness was then measured experimentally using the IFM and the RMS roughness was determined to be $\sigma = 46$ nm. Using the simulated 60 nm roughness the attenuation of a waveguide with a 90° bend was successfully estimated within the standard deviation of the fabricated waveguides. The correlation coefficient of the simulation being 0.9633 and the mean square error being 0.0370 $\mu$m$^2$. These results demonstrate that the sidewall roughness can be

modeled using the beam propagation method and the maximum sidewall roughness a waveguide can have is 80 nm RMS to get under a 0.08 dB/cm attenuation. Further the results indicate that when the sidewall roughness of a waveguide is 60 $\mu$m a bend radius of 0.6 cm is needed to achieve a bend loss of less than 0.7 dB.

# 4 Modeling In-Plane Performance of Single Mode Wavegudies

## 4.1 Single Mode Waveguides Criteria

One of the greatest advantages of a single mode optical waveguide is that it is able to support wavelength division multiplexing [39, 40, 41]. This allows the bandwidth of the waveguide to increase by allowing several different wavelength channels on one waveguide, effectively increasing the bandwidth by a factor of the number of channels. Adding and dropping one of these channels on the waveguide usually requires a ring resonator or a grating diffractive element.

To manufacture single mode waveguides a maximum size must be met so that only one mode can exist as explained in Section 2.1. A smaller waveguide is more difficult to couple light into the waveguide due to its size. The waveguide may be smaller than the maximum size, but the smaller size leads to more losses. Increasingly smaller waveguides are less desirable because the mode in the waveguide is less confined with the majority of modal structure is in the cladding. This causes more losses when bending the light in a short radius turn, as the weak confinement cannot contain the mode. This also causes more losses in sidewall roughness because the electric field interacts with the sidewall at a higher point on the modal curve than when the mode is more confined.

Single mode technology is not as far along in the development process as the multimode waveguides. This means single mode waveguides have more than one wavelength under consideration. Wavelength bands of 1310 nm and 1550 nm are also under consideration along with the 850 nm that multimode waveguides have. Wavelengths of 1310 nm and 1550 nm are the standard telecommunication wavelengths, the source and receiver are more costly but allow for larger waveguide dimensions.

The width of a rectangular (3D) dielectric waveguide the maximum width does not have a closed form solution and must be approximated [42]. One of the least complex approximations can be

made using the effective index method. The effective index method uses the width of a single mode planar (2D) dielectric waveguide and is limited by:

$$w_{planar} = \frac{\lambda}{2\,NA} \tag{57}$$

The mode that is supported by this waveguide is has the effective index

$$n_{eff} = \frac{\beta_m}{k_0} \tag{58}$$

Where $\beta_m$ is the speed of the propagation mode as shown in Section 2.2.3. The equation for the size of the waveguide can then be expressed as:

$$w_{rect} = \frac{\lambda}{2\sqrt{n_{eff}^2 - n_{clad}^2}} \tag{59}$$

A general approximation of this equation is

$$w_{rect} = \sqrt{2}\, w_{planar} \tag{60}$$

These estimates give a first order approximation to the maximum size of the waveguide [42], but when designing a waveguide a greater accuracy is usually required. To model the maximum size of the waveguide, COMSOL was used. COMSOL is a multiphysics program that can solve the equations given in Section 2.2.3 by discretizing the index profile along the waveguide then applying boundary conditions:

$$\vec{E}_{boundary} = 0 \tag{61}$$

$$\frac{\partial \vec{E}_{boundary}}{\partial \vec{n}_{boundary}} = 0 \tag{62}$$

$$\vec{H}_{boundary} = 0 \tag{63}$$

$$\frac{\partial \vec{H}_{boundary}}{\partial \vec{n}_{boundary}} = 0 \tag{64}$$

$$\tag{65}$$

The Helmholtz equation can then be solved for eigenvalue from an initial guess of the effective index.

$$\lambda = -j\,\beta. \tag{66}$$

The effective index guess is then updated until the determinate of the matrix system is zero. The results, shown in Figure 17, shows the structure of the waveguide mode along with its effective index.

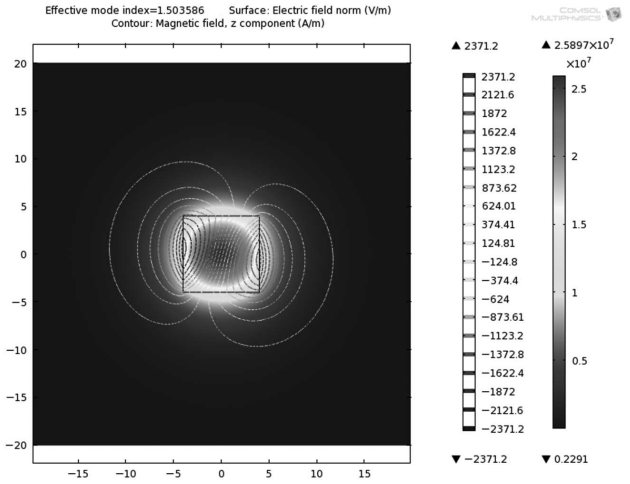


Figure 17: Comsol modeling of waveguide mode.

If the initial guess for the effective index is closer to the cladding index than the core index, the

chances of obtaining the highest mode is increased. If the initial guess is too close to the cladding index, however, a radiation mode, or a mode that does not confine the light, will be obtained. The best initial guess that was found was

$$n_{guess} = n_{clad}\left(1 + 0.3\frac{n_{core}}{n_{clad}}\right) \tag{67}$$

Figure 18 shows the effective index using the initial guess found in Equation 67.

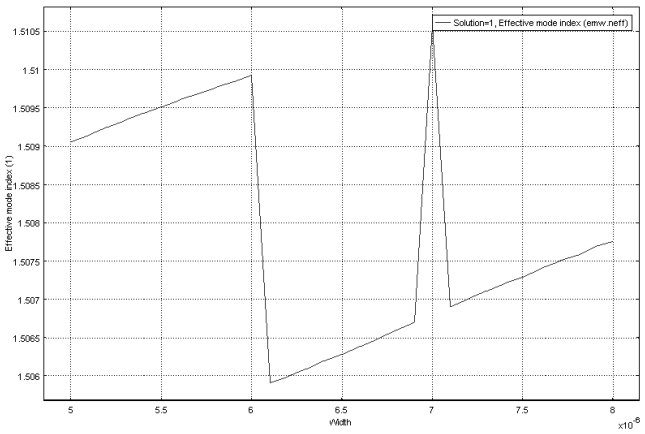


Figure 18: Effective index of highest order mode.

Figure 18 shows the effective index of the highest order mode. When the effective index approaches the cladding index, the waveguide is considered multimode. In this way, given a core and cladding index the waveguide size can be maximized to minimize coupling loss, sidewall loss, and bend loss.

The multimode material provided by Dow Corning has an core index of 1.52 and a cladding index of 1.50. The index contrast of these two material makes the maximum size of the waveguide 1.87 $\mu$m. This size is small compared to regular single mode fibers that are used to couple light into a fiber which have the size of around 7.5 $\mu$m, so high coupling losses arise. To couple light into the waveguide a Dow Corning SMF 28 was used. The numerical aperture of this fiber is 0.14. To minimize coupling losses the NA should be similar to the input/output fiber, thus reducing

coupling loss. Therefore, the material used to make single mode waveguides needs to be different than the material used for the multimode waveguides. A new experimental single mode material was obtained from Dow Corning. For a wavelength of 1550 nm, Dow Corning reported that the experimental material had an index of refraction for the core as 1.5061 for the core and 1.5015 for the cladding. Assuming numerical aperture of the waveguide remains unchanged for the 850 nm and 1310 nm wavelengths, the minimum waveguide size for rectangular dielectric waveguides is shown in Table 3.

Table 3: Maximum waveguide size for single mode criteria.

| Wavelength | 850 nm | 1310 nm | 1550 nm |
|---|---|---|---|
| Planar Approximation | 5.110 $\mu$m | 7.88 $\mu$m | 9.318 $\mu$m |
| COMSOL modeling | 4.875 $\mu$m | 7.75 $\mu$m | 8.875 $\mu$m |

A lithographic mask was designed so that the size of the waveguides with the 90° bends were 8 $\mu$m. This size allowed the waveguide to be single mode for the wavelength of 1550 nm with enough size tolerance to allow for slight changes in the index of refraction of the core and the clad and added size due to diffraction effects when patterning using the lithographic mask.

## 4.2 Minimum Sampling Conditions Needed for Single Mode BPM Simulations

To determine optimal sampling spacing criteria, a simple spacing convergence simulation was run. Figure 19 shows the effect of different sized sampling conditions. This simulation was a 2D straight BPM simulation with no roughness simulated in the waveguide. From this simulation it was found that the attenuation of the simulated straight waveguide changed very little (<0 .01 dB change) within the optimal sampling region. The losses started to vary more when the lateral sampling spacing exceeded 0.2 $\mu$m and the direction of propagation sampling spacing exceeded 0.4 $\mu$m. It was also found that if the propagation sample spacing was too small compared to the lateral sample spacing, stability issues occurred. This is likely due to the inability of the field to propagate in the lateral direction fast enough. Using the results of this simulation, it

was found that the optimal sampling conditions for single mode waveguides are 0.3 $\mu$m in the propagation and 0.1 $\mu$m in the lateral direction. The propagation direction sampling decreased from the multimode case from where the sampling was 0.7 $\mu$m in the propagation direction and the lateral was still unchanged at 0.1 $\mu$m.

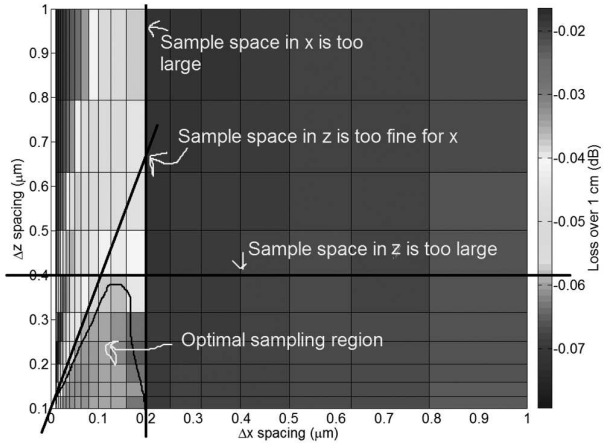


Figure 19: Effects of sample spacing in a 2D single mode straight waveguide with no roughness.

The convergence simulation was then re-run to show the effect of stability on a straight waveguide that has lithographic roughness. The simulation was performed using the roughness found for multimode waveguides or $\sigma = 60$ nm. As seen in Figure 20, even though the roughness at the side of the waveguide was under the size of the sampling conditions, the simulations showed little deviation from the no-roughness simulation. This could be due to how the simulation interprets sample region that are not uniform.

## 4.3 Minimum Cladding Size Conditions

When a waveguide is in close proximity to an electric conductor, such as copper, the field of the waveguide can interact with the conductor. This can lead to modes that can propagate within the cladding, attenuation of the field in the waveguide, and other non desired factors. A 2D BPM simulation was preformed to shows the interaction with a copper conductor. The simulation propagated for 1 cm. The modal structure was also observed at the end of the

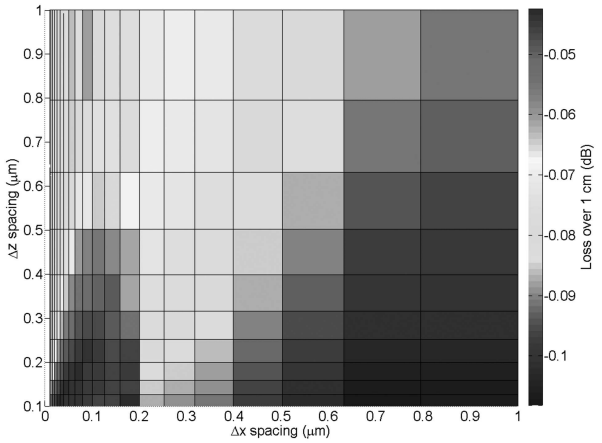


Figure 20: Effects of sample spacing in a 2D single mode straight waveguide with roughness

simulation to determine if any cladding modes were present. Figure 21 shows the minimum cladding width required on the top and the bottom of the waveguide to negate attenuation due to field interactions with copper traces at the wavelength of 1550 nm. When the cladding is 7 $\mu$m thick on the top and the bottom the waveguide has very little interaction with the copper traces.

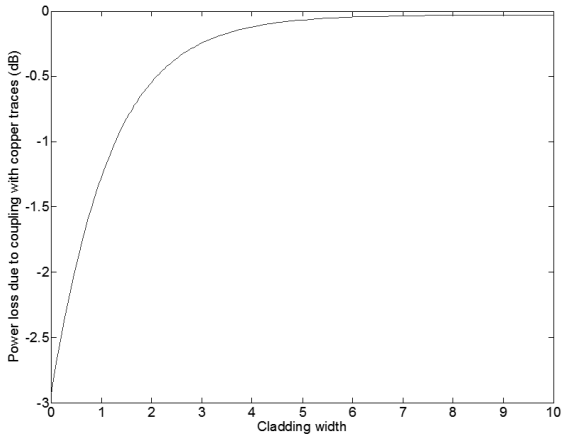


Figure 21: Minimum cladding width.

As explained in Section 2.2.3, each mode has a tail in the cladding. If one waveguide gets too close to another waveguide power from the tail of one waveguide can couple into the power in

the other waveguide leading to crosstalk. The minimum separation distance between two parallel waveguides is needed. Figure 22 shows channel isolation based on waveguide separation. Two 10 cm long parallel waveguides were simulated to determine how much power gets coupled from one waveguide to another. The simulation was run for a longer distance than the previous top cladding width simulation because power can easily couple from one waveguide to another if they have similar indices of refraction. The minimum waveguide spacing in order to achieve 40 dB of isolation must be 19.5 $\mu$m, 15.5 $\mu$m and 9 $\mu$m for wavelengths of 1550 nm, 1310 nm and 850 nm respectively.

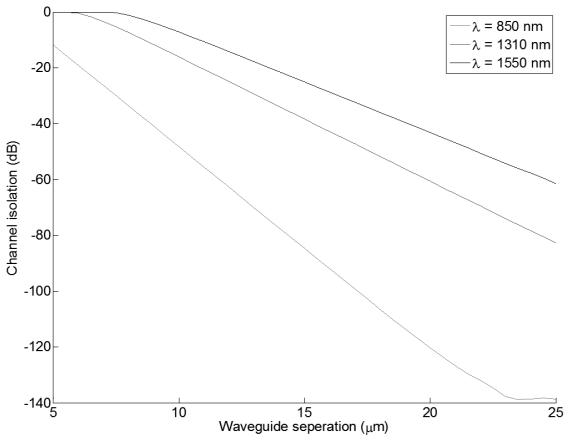


Figure 22: Channel cross-talk separation.

## 4.4 Attenuation due to Sidewall Roughness

The effect of sidewall roughness on the attenuation of the waveguides for the wavelengths of 1550 nm, 1310 nm, and 850 nm was calculated and the results are shown in Figure 23. Waveguides widths for 8, 10, and 12 $\mu$m were simulated. At these widths only the 8 $\mu$m at $\lambda = 1550$ nm is single mode, however, to match up with the manufactured data the larger sizes were simulated. The material absorption for the simulations was 0.05, 0.40, and 0.70 for wavelengths of 850 nm, 1350 nm, and 1550 nm respectively. Material absorption for the Dow Corning single mode material was unknown. Therefore, this was estimated based on Dow Cornings ©OE-4140 and OE-4141 multimode waveguides.

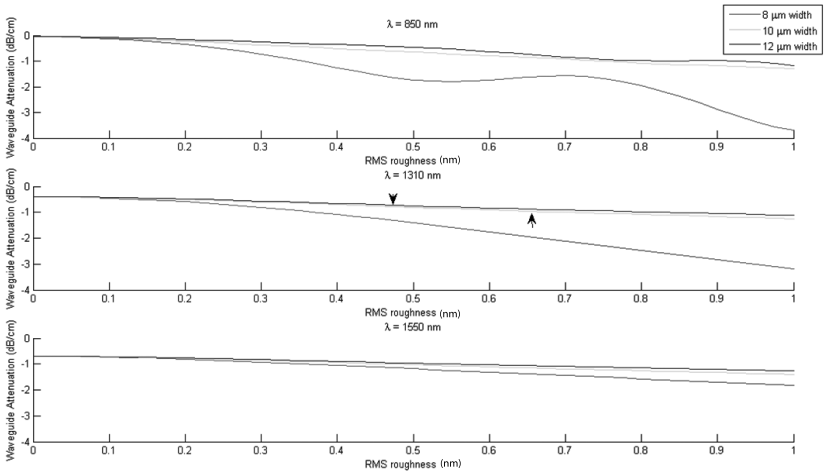


Figure 23: Effects of sidewall roughness on the attenuation of single mode waveguides.

The simulation shows that in larger wavelengths, the effect of lithographic roughness is lessened. Differences between the 10 $\mu$m and the 12 $\mu$m attenuation was less than expected while the 8 $\mu$m waveguide diverged from the larger guides faster, even when the waveguide was not multimode. This is likely due to the number of modes supported in the waveguide.

When manufacturing multimode waveguides, the root mean squared (RMS) sidewall roughness is between 40 nm and 60 nm. Because of the similar processing steps single mode waveguide roughness will be similar. Simulated results showed that for the single mode case the lithographic roughness was between 400 and 700 nm while the roughness for the 1550 nm wavelength was above 1000 nm. Measured waveguide attenuation is for the 1350 nm wavelength is shown by the arrows on the graph. These are unrealistic numbers. The discrepancy was found to be caused by material problems such as micro-voids or micro-cracks.

## 4.5 Simulation of Power Performance in Waveguides with Bends

The lower the index contrast is, the less confined the wave is to the waveguide. In a straight waveguide this makes little difference, however, when a bend in the waveguide is required the index contrast greatly affects the minimum turn radius. Figure 24 shows the effect of index

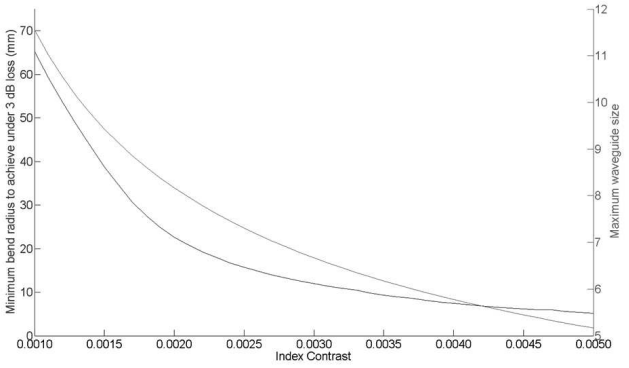


Figure 24: Effect of index contrast on single mode waveguide bends.

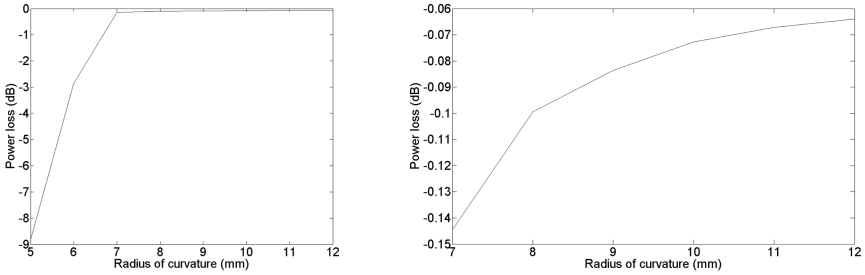


(a) Plot showing full loss.

(b) Plot zoomed in.

Figure 25: Bend waveguide power losses for index contrast 0.0046.

contrast that the index contrast has on the minimum bend radius.

In Figure 24 it was clear that an index contrast above 0.004 is necessary. Currently Dow Corning has a material that has an index contrast of 0.0046 at a wavelength of 1554 nm. Using these numbers the power losses for different radii bends are shown in Figure 25a which is magnified, in Figure 25b. The minimum bend radius was found to be at least 8 mm.

The modal structure of a waveguide bend has more power on the outside of the waveguide bend as shown in Figure 26. To get better power coupling from a straight waveguide to a curved waveguide, it is recommended to offset the two to get more efficient coupling in the overlap integral given in Equation 22 [43]. The structure of this offset is shown in Figure 27a. By evaluating the optimal overlap integral, the optimal offsets can be found. The optimal offsets are shown in Figure 27b.

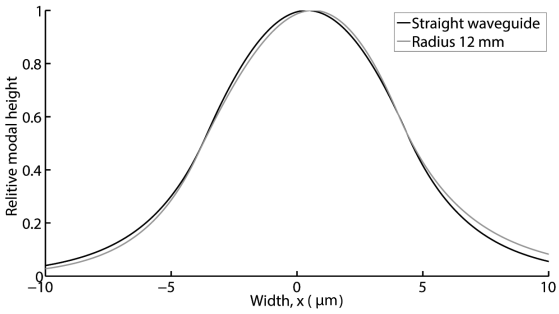


Figure 26: Comparison of modal structures between straight and curved waveguides.

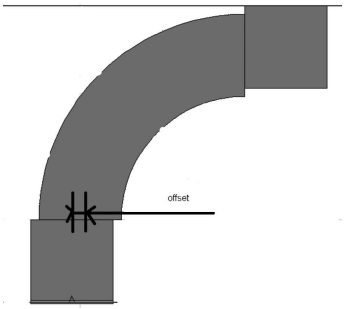


(a) Bend offset setup.

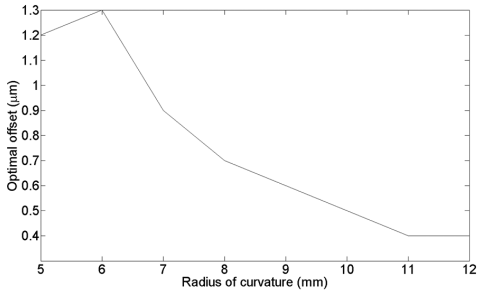


(b) Optimal bend offsets.

Figure 27: Offset to minimize the bending coupling losses.

## 4.6 Conclusion

Manufacturing parameters for single mode waveguides for use in printed circuit boards were found. Single mode waveguides are desirable in optical circuit board interconnection because they are not limited by modal dispersion, they have a smaller size, and wavelength division multiplexing is possible. The index of refraction of a polymer single mode waveguide manufactured by Dow Corning is 1.5061 for the cladding and the core index is 1.5015, the maximum size possible of the waveguide to be considered single mode is 4.875 $\mu$m, 7.75 $\mu$m, and 8.875 $\mu$m for a wavelengths of 850 nm, 1310 nm, and 1550 nm respectively. The waveguides were modeled in RSOFT using the beam propagation method. The optimal sampling size of the simulation was 0.1 $\mu$m in the transverse direction of propagation and 0.3 $\mu$m in the propagation direction. The minimum cladding on the top and the bottom of the waveguide was 8 $\mu$m and the minimum separation distance was 19.5 $\mu$m, 15.5 $\mu$m, and 9 $\mu$m for wavelengths of 1550 nm, 1310 nm and

850 nm respectively. The minimum sized radius of curvature of the waveguide was found to be 8 mm.

# 5 Multimode Vertical Interconnect Assembly

In order to fully realize the full potential of optical waveguides in optical printed circuit boards, the problem of how to couple light into the waveguide needs to be addressed. This interconnect couples light from another fiber or a VSCEL into the waveguide. This can be as simple as butt coupling to the waveguide edge done previously when testing the waveguides. However, this method is not conducive to optical interconnect systems in which opti-electric circuit boards are manufactured. Turning light out of plane to another layer of the circuit board, or to an optical receiver mounted on top of the circuit board, becomes necessary. To accomplish this an optical vertical interconnect assembly (VIA) needs to be manufactured. A proposed VIA is shown in Figure 28a. This is a lensed VIA that contains a total internal reflection mirror end face to the assembly.

When manufacturing the VIA it was found that the power varies drastically when the distance, $D$, is changed as is shown in Figure 28b. The power change is a consequence of the output field changing with the length of the waveguide as shown in Figure 29. The changing field makes placing the VIA very difficult for the manufacturer of the waveguides. Finding the optimal position, $D$, requires knowing the modal structure of the terminated waveguide. Simulating the exact modal structure for a waveguide is a modeling intensive process which requires knowledge of many waveguide parameters such as waveguide length, curves, and crossings. To alleviate this constraint, the optimal VIA placement is found for all possible VIA lengths, $L$.

## 5.1 Multimode Coupling

The size of the embedded multimodal waveguides allows for greater mechanical misalignment and fabrication tolerance when compared to single mode waveguides. As a consequence, multimode waveguides can contain thousands of modes, each mode distributing the total power of the waveguide [44]. Additionally, these modes travel at different speeds, resulting in modal dispersion. Since the phase of each mode moves at a different speed the electric field distribution changes depending on the length of the guide. This self-imaging principle of multimode waveguides [45]

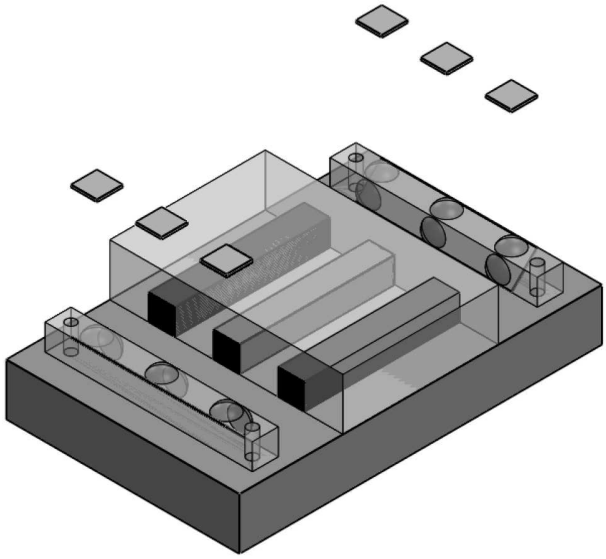

(a) Isometric view.

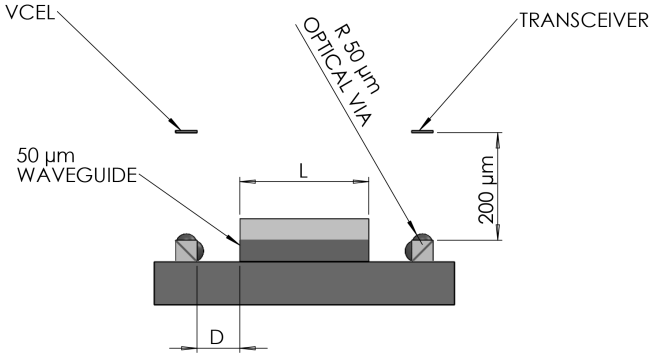


(b) Front view.

Figure 28: Optical VIA placement in waveguide layer.

is shown in Figure 29.

The self imaging principle changes the output profile in the angular spectrum, resulting in different coupling efficiencies of the VIA structure, especially when the transceiver is within the near field [46]:

$$z < \frac{2P^2}{\lambda} \tag{68}$$

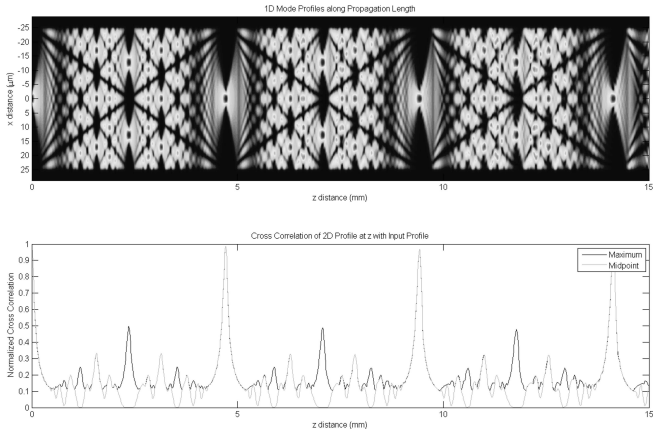


Figure 29: Repeating mode length.

where $P$ is the aperture dimension. For example, two output fields from two different lengths of waveguides are given in Figure 30a and Figure 30b. Using a transceiver size around 50 $\mu$m results in massively different coupling efficiency between the two lengths.

A designer can find the optimal coupling position for one of these waveguides, but embedded multimode waveguides in printed wiring boards can have several parallel channels utilizing one VIA, as shown in Figure 28a. If one channel of a waveguide group is slightly longer than the other waveguides in the group, its coupling efficiency can be significantly less (1-6 dB) than its neighbors leading to that channel exceeding the overall link budget. A change in index of refraction from heating of the board or aging of the material would additionally impact the coupling efficiency [47]. If the refractive index of the waveguide changes by 0.01, the optical path length changes by 1 mm per 10 cm length, resulting in a new modal structure that is coupled to the optical VIA changing the coupling efficiency appreciably on the order of 1-6 dB.

An optical electrical printed wiring board section is shown in Figure 28a and Figure 28b to indicate how the VIA is located within the embedded waveguide layer. The optical VIA consists of a molded block of Polymethyl methacrylate (PMMA). The index of refraction, (n = 1.41), allows for a 45° total internal reflection mirror to turn the light 90°. There are two 50 $\mu$m curvature lenses, separated by an optical path length of 70 $\mu$m, located at the entrance and exit of the optical channel. Approximating that the total internal reflection mirror is a perfect mirror,

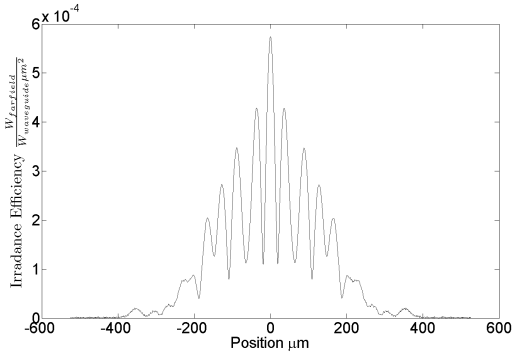


(a) $L = 1.5$ mm.

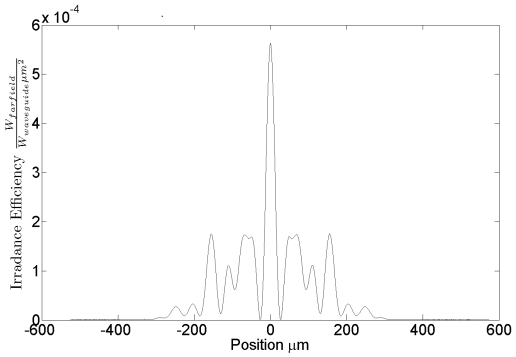


(b) $L = 2.0$ mm.

Figure 30: Output irradiance patterns 1.5 mm away from the waveguide.

the overall effective focal length of the system is 76.5 $\mu$m.

To find the optical coupling loss of the VIA, two simulation parameters were changed. First, varying waveguide field outputs that are dependent upon the length of the waveguide were modeled using the beam propagation method. Then, the efficiency through the VIA was modeled for each length of waveguide ($L$). This process was repeated for different waveguide end to VIA distance, $D$, ranging from 50 $\mu$m to 150 $\mu$m, which was chosen to reflect the dimensions of the milled waveguide trenches.

## 5.2 System Layout

The field distributions for each length of waveguides were found by modeling a 50 $\mu$m x 50 $\mu$m embedded step index square waveguide. The setup for the simulation is shown in Figure 31. The beam propagation method was used to find the field distribution for each length, $L$, of waveguide. This method is applicable because the field amplitude slowly varies in the propagation direction [48]. Simple transparent boundary conditions were used [31] because they are most suited for highly multimode problems [32]. An additional absorbing layer with a width of 12.5 $\mu$m was added to ensure field falloff of the model. The index of the core of the material is 1.52 and the cladding index is 1.50. These indicies were chosen to match Dow Corning's ©OE414x polymer waveguide material. The input of the simulation was a 5.6 $\mu$m single mode fiber. The numerical aperture of the fiber was 0.24 and illuminated the waveguide with 1 mW of light. This was chosen because it was assumed that the VCSEL or single mode fiber input shown in Figure 28b was mirrored onto the waveguide face. The field was first propagated 1 mm to ensure mode coupling losses were taken into account. The field output was sampled every 10 $\mu$m until the field had repeated itself, as shown in Figure 29. A summary of the simulation parameters is given in Table 1.

Using the calculated field distribution outputs, the light was propagated through the VIA assembly using an angular spectrum propagator, as shown in Section 2.2.4. After propagation to the lens, the angular spectrum becomes:

$$U(x,y,z) = \mathcal{F}\left(L(x,y)\,\mathcal{F}^{-1}\left(U(f_x,f_y,0)\,e^{\frac{2\pi z}{\lambda}\sqrt{1-(f_x\lambda)^2-(f_y\lambda)^2}}\right)\right) \tag{69}$$

$L(x,y)$ is the contribution of an aberration free lens defined by [49]:

$$L(x,y) = \frac{f^2}{x^2+y^2+f^2}\,e^{j\,\frac{2\pi z}{\lambda}\left(\sqrt{x^2+y^2+f^2}-f\right)}\,T_x(x,y)\,e^{j2\pi\,(f_x\,x+f_y\,y)} \tag{70}$$

Where $T_x$ is the reflection coefficient at the lens boundary and $f$ is the focus of the lens. The

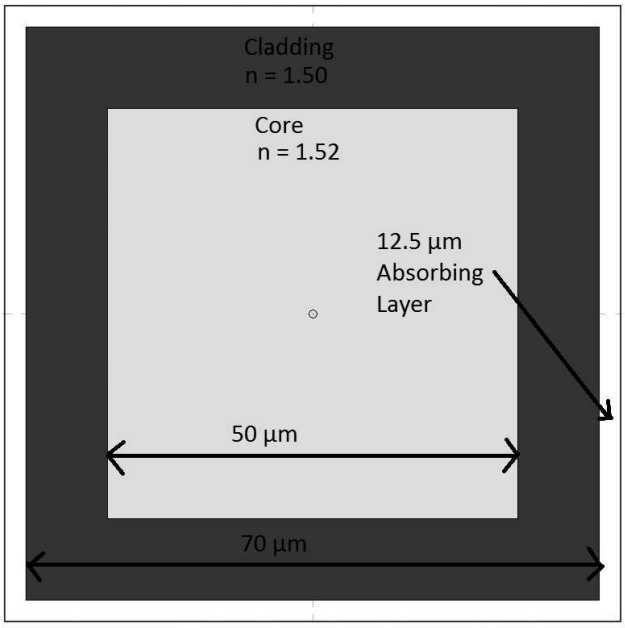


Figure 31: Buried waveguide setup for BPM simulation.

setup for determining the reflection coefficient of the lens is shown in Figure 32. In determining the reflection coefficient, it is assumed that all the light incident upon the lens is parallel to the optical axis, or $\phi = 0$, (paraxial assumption). This assumption is valid because the reflection coefficient, $R$, is roughly the same for small angles of $\phi$, or $\frac{dR}{d\phi} \approx 0$ for small angles of phi.

The angle of incidence to the air lens boundary can then be simplified to:

$$\Theta = \arcsin(\frac{\hat{r}}{R}) \tag{71}$$

Where $r$ is the height of the incident parallel ray and R is the radius of the lens. To determine an paraxial transmission coefficient, it is also assumed that all the light hitting the VIA is randomly polarized.

The input field, the lens, and output field must be sampled at:

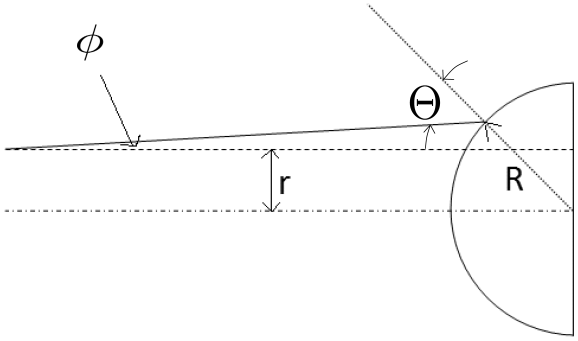


Figure 32: Setup for determining reflection coefficient, Tx.

$$N_{x,y} = \frac{2\lambda z}{dx^2} \tag{72}$$

Which is double as reported in to the sampling size given by Odate [49] but is needed to satisfy Nyquist criterion. Where $z$ is the overall optical path length. For most lens systems this criterion leads to unrealistic array sizes and run times, but in the case of microlenses, such as the VIA, this application is efficient [50], giving a runtime of 10 minutes.

All the field outputs generated from the beam propagation method were then put through the lens system of the optical VIA shown in Figure 33. In the optical system the optimal coupler position, $D$, is sampled as 21 different free space propagation portions of length between 50 and 150 $\mu$m in increments of 5 $\mu$m. The output field then encounters the first lens and travels 70 $\mu$m in an index of 1.41. Finally, a third simulation was run propagating the field from the second lens interface 200 $\mu$m to the 50 $\mu$m square sensor. The power on the detector compared to the power from the waveguide output is defined as the system efficiency.

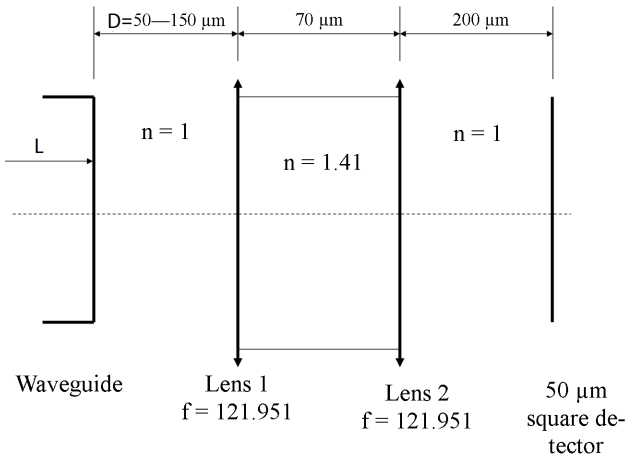


Figure 33: Optical setup for propagating a field through the VIA.

## 5.3 Analysis

Figure 34 shows two samples of how the coupling efficiency of the VIA assembly changes depending on the length of the waveguide. The attenuation of both waveguide to VIA distances shows significant differences in efficiency depending on the waveguide length, $L$, although there is a relativity small difference between the two lengths, $D$. To determine the optimal VIA placement distance, three metrics were used to determine the optimal placement of the VIA, the highest average power, the lowest variance, and the worst-case scenario.

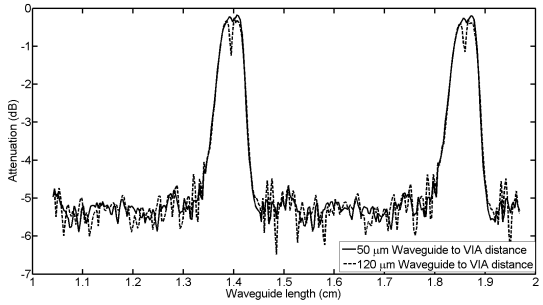


Figure 34: Attenuation of VIA assembly for two waveguide to VIA lengths.

The first metric was obtaining the optimal waveguide to VIA distance based on the average power of the all the waveguide lengths. The attenuation of the distance the VIA is away from

the waveguide end-face, $D$, distance is shown in Figure 35. The optimal placement for the VIA using this metric was 150 $\mu$m away from the waveguide. This result is intriguing because when using geometrical optics the optimal focal point appears at 123.9 $\mu$m. A possible reason for the difference may be the beam waist for each mode will be slightly different, resulting in a circle of least confusion and not a true focal point.

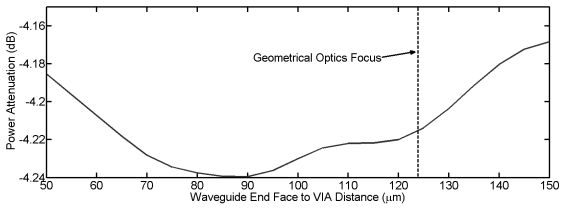


Figure 35: Average power of VIA assembly.

The second metric was the variance of the power in the VIA assembly. Minimizing the variance of the system also minimizes the number of waveguide channels that are deemed out of tolerance. Figure 36 shows the variance depending on the waveguide to VIA distance. The optimal placement of the VIA using this metric is also 150 $\mu$m. This metric gives the same optimal coupling position as the average power simulations.

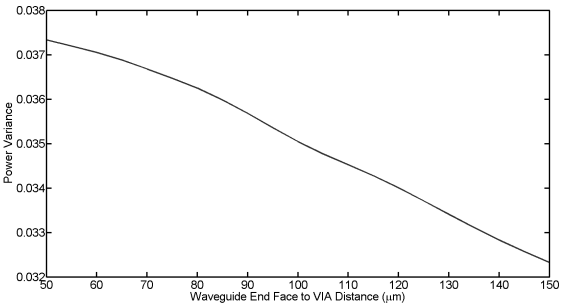


Figure 36: Variance in power of VIA assembly.

The last metric found the lowest attenuation with the worst-case waveguide length distance, or the optimal distance using the worst-case scenario. This metric is important in minimizing the number of waveguides that are deemed out of tolerance in a multichannel optical VIA. The results for the simulation are shown in Figure 37. The optimal distance with this metric is 60 $\mu$m with an attenuation of 5.85 dB.

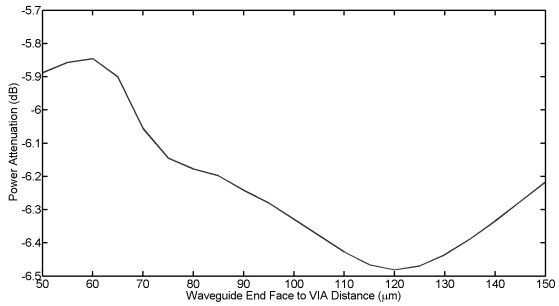


Figure 37: Worst case attenuation of VIA assembly.

## 5.4 Conclusion

To determine the optical loss in an optical VIA for embedded multimode waveguide applications, a single mode fiber input was propagated along a 20 mm waveguide in order to mimic field structures present at the output. The single mode input was launched into a 50 $\mu$m square multimode structure. Losses for the system ranged between 0.177 dB to 6.48 dB. For optimal VIA placement that, on average, couples effectively or has the smallest variation with respect to changes in the waveguide attenuation, the VIA placement should be just beyond geometrical optics optimal focal point at 150 $\mu$m away from the end of the waveguide. To have the least amount of coupling loss for all waveguide distances, the VIA should be placed before the geometrical optical optimal focal point at 60 $\mu$m away from the end of the waveguide. Using these metrics it is possible to blind pick and place a waveguide VIA in the optical printed circuit board process so that the attenuation or variance of the waveguide channels of the VIA assembly is minimized.

# 6 Single Mode Grating Vertical Interconnect Assembly

As explained in Section 1, silicon waveguides suffer from high attenuation. This makes them impractical for passive bus communications because of the high expense. Combining single mode polymer waveguides and silicon waveguides into a hybrid technology alleviates this problem. This solution uses silicon waveguides for the integrated optics, then it uses, low loss single mode waveguides for transferring information. To create the hybrid solution, both the silicon waveguides and the single mode waveguides must be able to connect to each other through an optical vertical interconnect assembly.

Coupling waveguides with two very large numerical aperture differences is a very lossy process. A problem that arises with the coupling of the two technologies is the massive numerical aperture mismatch. Silicon waveguides consist of a silicon core with a silicon dioxide cladding on the outside of the waveguide. The index of silicon at $\lambda = 1310$ nm is 3.503 [51] for the core and 1.531 for the cladding [52]. This gives a numerical aperture shown in Equation 25 of 3.15. Using the equation

$$NA_{waveguide} = n_{med} \sin(\theta) \tag{73}$$

Where $\theta$ is maximum output angle in a given medium with index $n_{med}$. The numerical aperture of 3.13 gives an imaginary output angle in air making the waveguide output in a full $2\pi$ steradians as was shown in Figure 38. Whereas the single mode waveguide manufactured by Dow Corning ©has a core index of 1.5135 and a cladding index of 1.5057 giving a numerical aperture of 0.153. This means that the single mode waveguide can only accept power from a very small portion of the power that the silicon waveguide outputs leading to heavy losses.

A possible solution to the problem is the utilization of a lensed coupler, as was done with the multimode waveguide. The single mode interconnects would give the advantage of consistent output throughout the waveguide because of the singular mode, eliminating the problem with multimode waveguide of a changing coupling efficiency. Unfortunately, this comes at the price

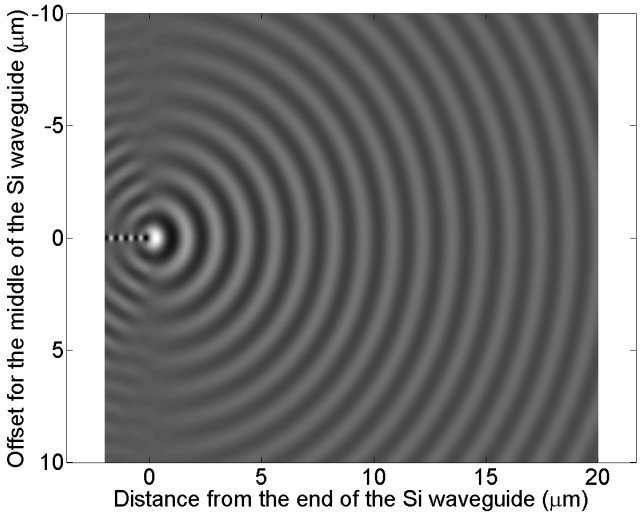


Figure 38: Output waveform at the end of a silicon waveguide.

of alignment tolerance when coupling into the waveguide. For example, if using a lensed system, the input tolerance will be stricter than butt coupling a single mode fiber and a single mode waveguide. The alignment tolerance for a fiber and a single mode waveguide is shown in Figure 39.

This tolerance of the single mode waveguide has a much greater limit as compared to the multi-mode waveguide butt coupling tolerance given in Figure 40.

The other difficulty with using a total internal refraction coupler is the size of the coupler needed to give decent coupling losses needs to have high numerical aperture lens to capture most of the light from the Si waveguide. Where the numerical aperture of the lens is given by

$$NA_{lens} = \frac{f}{D} \tag{74}$$

Where $f$ is the focal length of the lens and $D$ is the diameter of the lens.

Another possible solution to coupling the light into the single mode waveguide is to use a volume grating coupler. Volume grating couplers use a varying index contrast that is spaced in such a

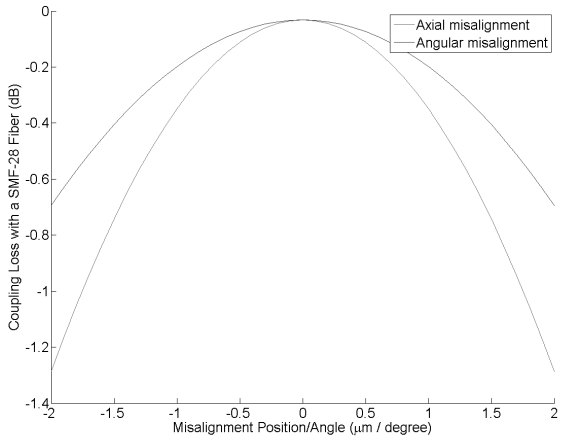


Figure 39: Axial and angular misalignment tolerances in a single mode waveguide butt coupled to a SMF 28 fiber.

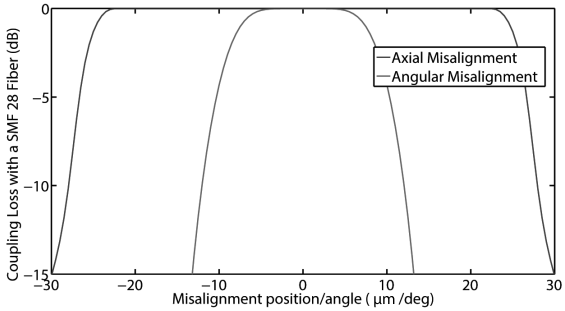


Figure 40: Axial and angular misalignment tolerances in a multimode waveguide butt coupled to a SMF 28 fiber.

way that the reflected light adds constructively. Designing the coupler in this way, the size of the coupler can be larger to give better coupling efficiencies

## 6.1 In-Plane Bragg Gratings

A basic Bragg grating has a periodic index characterized by:

$$n_{grating}(z) = n_{clad} + dn_{write}\,\Pi(\frac{z}{\Lambda}) \tag{75}$$

Where $dn_{write}$ is the index difference in the core depending on the intensity of the writing light, $\Lambda$ is the period of the index change, and $\Pi$ is the rectangular function given by:

$$\Pi(x) = \begin{cases} 0 & \text{if } x \, mod \, 1 > \frac{1}{2}, \\ \frac{1}{2} & \text{if } x \, mod \, 1 = \frac{1}{2}, \\ 1 & \text{if } x \, mod \, 1 < \frac{1}{2} \end{cases} \tag{76}$$

The grating structure is shown in Figure 41. Suppose the fundamental mode is propagating down a single mode waveguide is incident on the waveguide. The modal structure is characterized by

$$A(x, y, z) = a(x, y) \exp^{i\beta z} \tag{77}$$

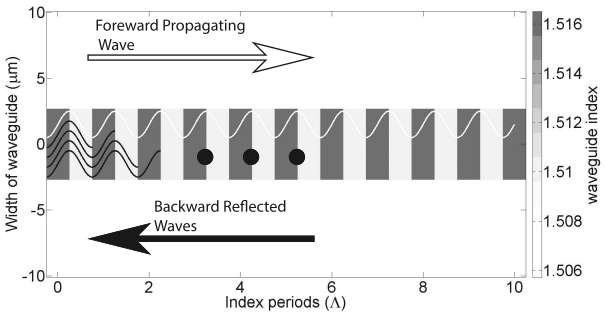


Figure 41: Basic waveguide grating.

When the index of a material changes, a portion of light is reflected back given by the Fresnel equations at normal incidence

$$\Gamma = \left| \frac{dn_{write}}{2\, n_{core} + dn_{write}} \right|^2 \tag{78}$$

When the change in the core index is large compared to the index of the core, the reflection coefficient approaches unity, but most of the time this is not an option and the change in the core index is relatively small. When using the single mode material from Dow Corning, each

interface reflects $8.556 * 10^{-4}$ of the incoming light. This makes for a very inefficient coupler. Many reflections can be made by adding the periodic interface . If the grating period $\Lambda$ is arranged in such a way that the phases of the reflected light add constructively, such as is shown in Figure 41, the steady state equation, or the equation that does not include dispersion effects, may be written as

$$\begin{aligned} A_{reflect}(x,y,z) &= \left(\Gamma + \Gamma(1-\Gamma) + \Gamma(1-\Gamma)^2 + \ldots\right) a(x,y) \exp^{-i\beta z} && (79) \\ &= \sum_{n=0}^{x} (\Gamma\,(1-\Gamma)^n)\, a(x,y) \exp^{-i\beta z} && (80) \\ &= (1-(1-\Gamma)^x + (1-\Gamma)^x\,\Gamma)\; a(x,y) \exp^{-i\beta z} && (81) \end{aligned}$$

Where $x$ is the number of reflections.

To make the reflections add up constructively, the time the wave takes to travel from one reflection boundary to the to the next reflection boundary and back must be a integer of the wavelength in the medium.

$$2 * \Lambda = m \frac{\lambda}{\bar{n}_{eff}} \tag{82}$$

Where $\bar{n}_{eff}$ is the average effective index of the waveguide which can be estimated in the first order by [53]

$$\bar{n}_{eff} = \sqrt{\frac{n_{eff_{low}}^2 + n_{eff_{high}}^2}{2}} \tag{83}$$

Where $n_{eff_{high}}$ and $n_{eff_{low}}$ is the effective index of the core material with and without the added index from overexposure respectively.

## 6.2 Slanted Bragg Grating

The inline Bragg grating is only effective when sending waves back down the grating and is not applicable for coupling. To couple light into and out of the grating, the grating must be angled as in Figure 42.

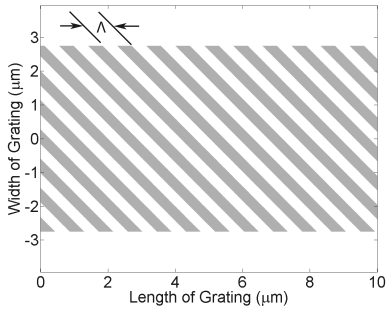


Figure 42: Slanted volume grating setup.

The process of adding the slanted interface is just an expansion on the previous straight grating. According to the Huygens - Fresnel principle, every point along a disturbance can be become a source of a spherical wave, as show in Figure 43. Applying the optical path difference constraint to the slanted grating gives an equation of

$$(AB + CB) - (AC') = m\frac{\lambda}{\bar{n}_{eff}} \tag{84}$$

Where

$$AB = BC = \frac{\Lambda}{\sin\theta} \tag{85}$$

$$AC = \frac{2\Lambda}{\tan\theta} \tag{86}$$

Giving

$$AC' = \frac{2\Lambda \cos^2 \theta}{\sin \theta} \tag{87}$$

Plugging these into Equation 84 yeilds

$$\Lambda = \frac{m\lambda}{2\,\bar{n}_{eff}\,\sin\theta} \tag{88}$$

Which is known as Bragg's law.

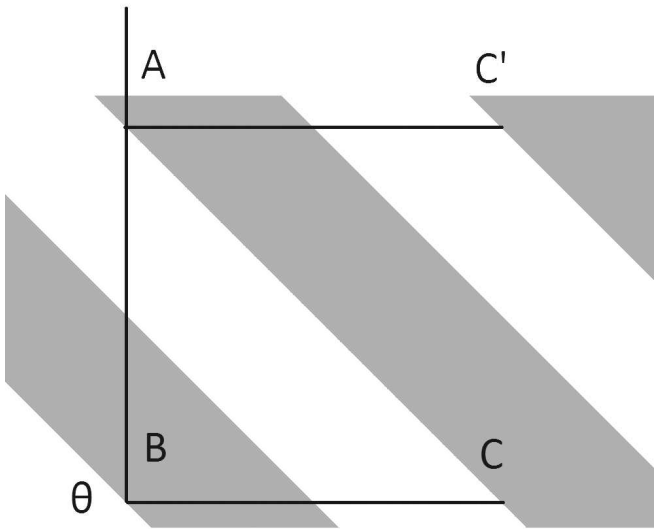


Figure 43: Bragg's effect setup for slanted volume grating.

Bragg's law can now be applied to a slanted grating coupler with an index modulation of

$$n_{grating}(x,z) = n_{clad} + dn_{write}\,\Pi(K \cdot (\hat{x} + \hat{z})) \tag{89}$$

With $K$ being the grating vector. The grating vector expresses the direction and the spacing of the grating interfaces. Using the conservation of momentum and the conservation of energy it can be shown that [54]

$$K = k_{in} - k_{out} \tag{90}$$

Where $k$ is the propagation vector

$$k_i = \frac{2\pi \bar{n}_i}{\lambda} \tag{91}$$

Applying Bragg's law to the grating vector for normal incidence, $k_{in} = -k_{out}$, the grating vector magnitude can be expressed as

$$|K| = \frac{2\pi}{\lambda} \tag{92}$$

The grating period $\Lambda$ and the grating angle $\theta$ can then be determined using Bragg's Law and the grating vector equation. Using Bragg's Law the grating vector along the propagation direction can be determined $K_z$

$$\Lambda_z = \frac{\lambda}{Sin(2\theta)\bar{n}_{eff}} \tag{93}$$

The grating vector equation now becomes

$$\sqrt{\left(\frac{2\pi}{\Lambda_z}\right)^2 + \left(\frac{2\pi}{\Lambda_x}\right)^2} = \frac{2\pi}{\lambda\, n_{core}} - \frac{2\pi}{\lambda\, \bar{n}_{eff}} \tag{94}$$

Where $\Lambda_x$ may be solved. The angle of the grating may now be solved as

$$\theta = \arcsin\left(\frac{K_x}{K_z}\right) = \arcsin\left(\frac{\Lambda_z}{\Lambda_x}\right) \tag{95}$$

Using Equations 93 and 95 it is possible to design a focusing grating that focuses light into a silicon waveguide by varying the grating vector, $K(x, z)$ and the grating angle $\theta(x, y)$ along the length of the waveguide. An example of a focusing grating is shown in Figure 44.

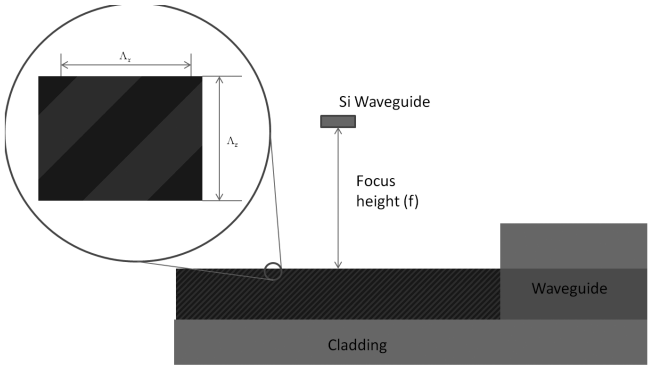


Figure 44: Waveguide containing a slanted volume grating.

## 6.3 Rigorous Coupled Wave Analysis

Equations 93 and 95 are used to solve for the grating period and the angle in the first order geometrical optics approximation. Since the wavelength of the input light, $\lambda$, is on the same order as the grating period, $\Lambda$, this approximation is not accurate and a wave optics approach needs to be used. One of the methods that may be used to solve the optimal grating period and angle using wave optics is rigorous coupled-wave analysis (RCWA) [55, 56, 57].

RCWA analysis assumes that the grating is infinite in the propagation direction, therefore, the grating's diffraction may be solved over one period of the grating as shown in Figure 45. The restriction to one unit cell means gives rise to a boundary condition on $\Gamma_2$ and $\Gamma_4$ given by the Floquet-Bloch theorem [58].

$$E(x, z) = E(x, z + \Lambda) \exp^{j \sin\theta}, \quad 0 \leq x < \Lambda, \quad -\infty < z < \infty \tag{96}$$

Therefore the outgoing wave condition only needs to hold for boundaries $\Gamma_1$ and $\Gamma_3$ or the reflected and transmitted waves respectively.

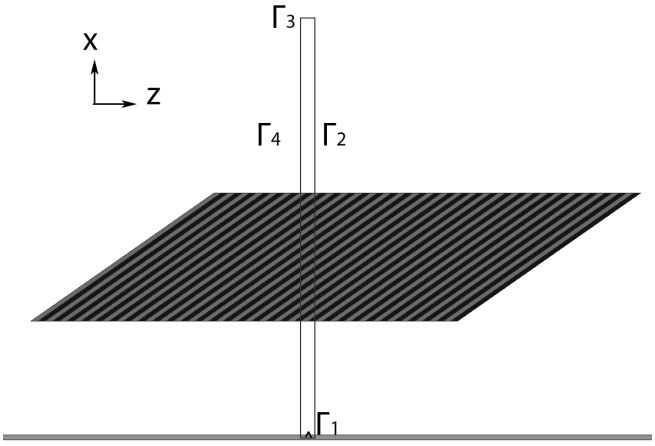


Figure 45: RCWA domain.

The index distribution is then sliced up in the $x$ direction, eliminating the $x$ direction dependency. It is then possible to model the $z$ direction index perturbation as a Fourier series expansion. Since the grating index profile is now continuous, the reflection can be found using the Helmholtz equation shown in Equation 18. Using the methods described in [55] the reflected electric field can be found for one layer. Propagating the transmitted wave to the next z layer the resulting electric field can be written as

$$E(x,z) = \sum_{x=-\infty}^{\infty} \left( A_m e^{jk_{xmb}x + jk_{mzb}z} + B_m e^{jk_{xmf}x + jk_{mzf}z} \right) \tag{97}$$

where $A_m$ is the reflected order coefficients, $B_m$ is the transmitted orders, and $k_{imd}$ is the direction coefficients.

## 6.4 Focusing Grating Design

Using RCWA it is possible to refine the new chirped grating period in the propagation direction ($\Lambda_z(z)$) and the transverse direction ($\Lambda_x(z)$) more accurately than the first order approximation. The optimal parameters for the RCWA optimized grating is shown in Figure 46.

In Figure 46 a grating profile that can be made based on total system design is shown. If the

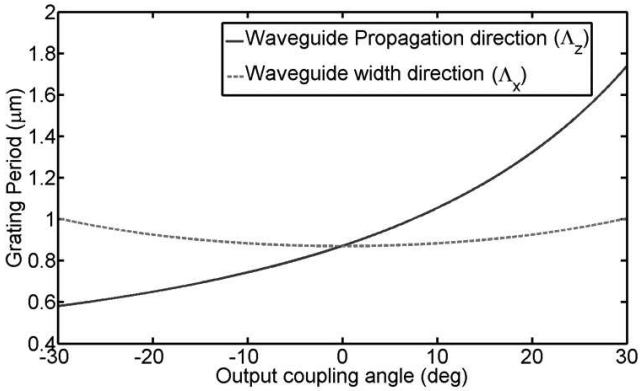


Figure 46: Optimal grating periods found using RCWA.

grating length is 500 $\mu$m and a focal distance is 1 mm the parameters of the grating coupler are shown in Figure 47.

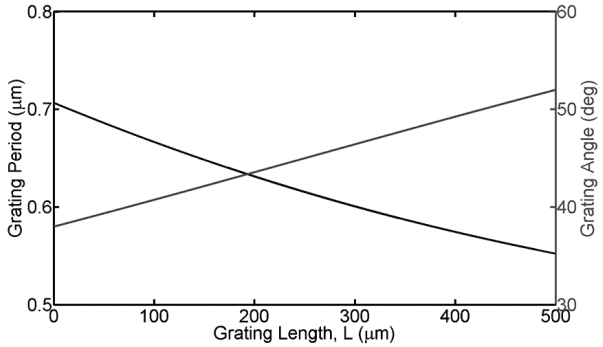


Figure 47: Grating period and angle derived from RCWA.

Along the length of the grating the grating period varies from 710 nm at the beginning of the grating to 570 nm at the end of the grating. The grating angle also varies from 51° at the beginning of the waveguide to 36° at the end of the waveguide. To simulate the efficiency of the waveguide, the finite difference time domain (FDTD) method was used. The FDTD model can be implemented in two different ways. In Figure 48a the grating interface is parallel to the simulation axis and in Figure 48b the sidewall of the waveguide is parallel to the simulation axis. The advantage of having the grating interface parallel to the simulation axis is that the field hits the grating interface perpendicularly, eliminating any higher grating modes that occur because of the simulation grid size. It also easier to make the grating profile as the $x$ dependency of the

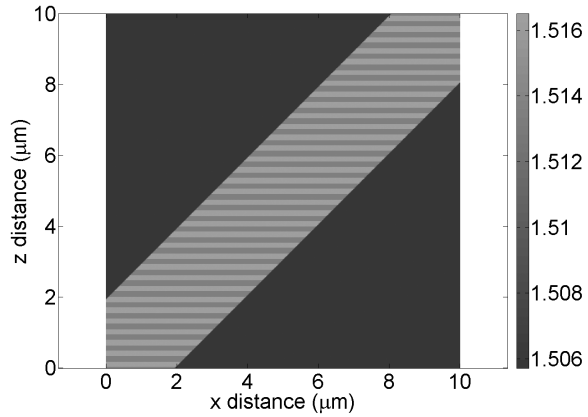


(a) FDTD model with grating parallel to simulation boundary.

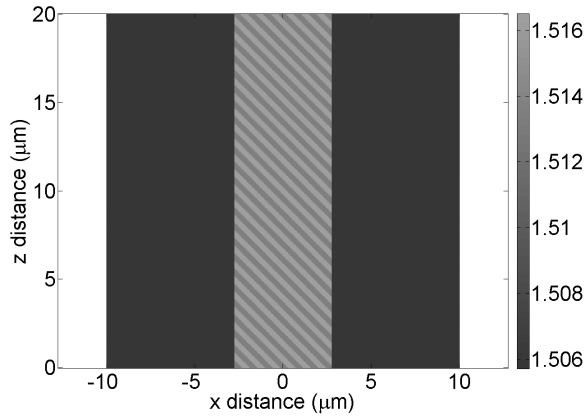


(b) FDTD model with sidewall parallel to simulation boundary.

Figure 48: Comparison of FDTD models.

grating is eliminated and the grating profile can be made in RSOFT without using an external meshing software. These advantages come at the cost of a larger simulation domain because of the sideways waveguide and the inability to make a grating that varies both grating period and grating angle.

Figure 49 shows the dependency of the sample size on the grating efficiency. When the sample size of the simulation is equal to or less than 0.04 $\mu$m, there is less than 0.1 dB difference in both the straight and angled simulations. The straight simulation took 82 hours to complete, while the angled simulation took 10 hours less, completing in 72 hours. This is surprising because the

angled simulation is considerably larger than the straight simulation. For a grating length of 500 $\mu$m, the simulation size for the angled simulation is 656.0 MB while the straight simulation is 151.4 MB. The difference in time is likely due to RSOFT needing to load the grating mesh for the straight waveguide multiple times during a simulation.

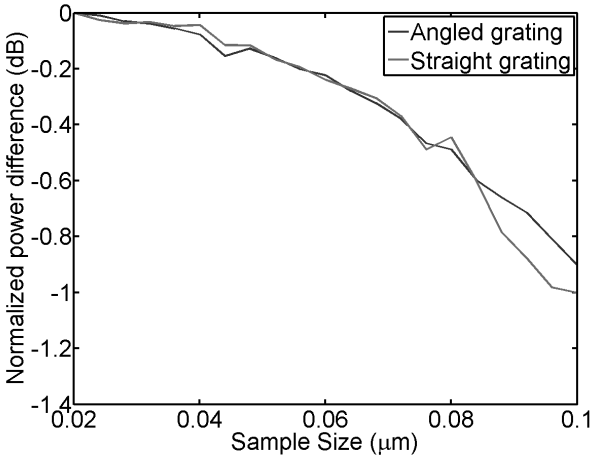


Figure 49: Grating FDTD sample size convergence.

Unfortunately, because of the changing grating period and grating angle, the straight simulation needed to be used for the simulation. A grating length of 500 $\mu$m and a focal length of 1 mm was used. The grating mesh for the coupler is shown in Figure 50.

Due to the low index contrast of the core material, the efficiency of the blazed and angled grating was low. Each of the slanted grating interfaces did not couple with each other leading to high loss. The FDTD simulation, shown in Figure 51, shows that almost no light couples into the waveguide, revealing a 14 dB loss for a 500 $\mu$m grating.

Other than the low efficiency, the deficiency with blazed and angled grating is that it is very difficult and time consuming to manufacture. Doing both the blazed and the angle grating requires that the grating be made with linear approximations of the grating vector. The grating can then be made with two cylindrical lenses and a prism using methods described in [59]. This method has the problem of the high alignment tolerance necessary to manufacture the grating. Other options for manufacturing the grating include micromolding the grating [60], but the

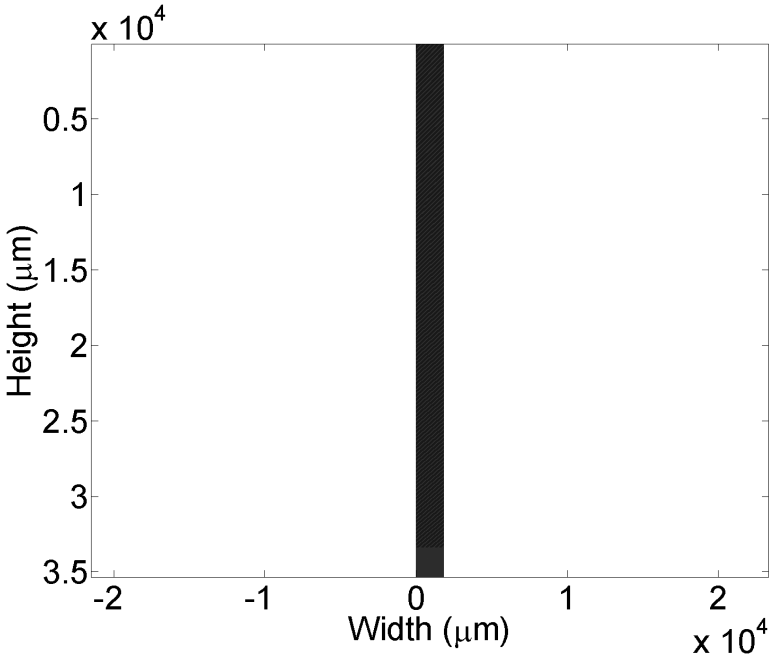


Figure 50: Grating mesh.

changing angle of the grating by large amounts may not release the grating and depositing a blazed grating [61] at a certain angle to a small section of the grating then changes the angle as the grating propagates. However, this process is time consuming and not applicable to mass manufacturing. Because the grating yields low efficiency and is time consuming to manufacture other methods for using grating couplers were needed.

## 6.5 Lensed Grating Design

To eliminate the need to make a blazed and angled grating, the light from the silicon waveguide needs to be collimated. To collimate the light into the grating a lens micromolded into the core of the waveguide is proposed, as shown in Figure 52. This design has several advantages over the focusing grating. The lensed grating can be manufactured by interfering two coherent laser beams and a prism [62, 63]. Each of the lens grating periods is at the perfect angle and grating period, leading to higher coupling efficiency. Finally, the lensed grating has a lager alignment tolerance than the focusing grating, making it easier to manufacture.

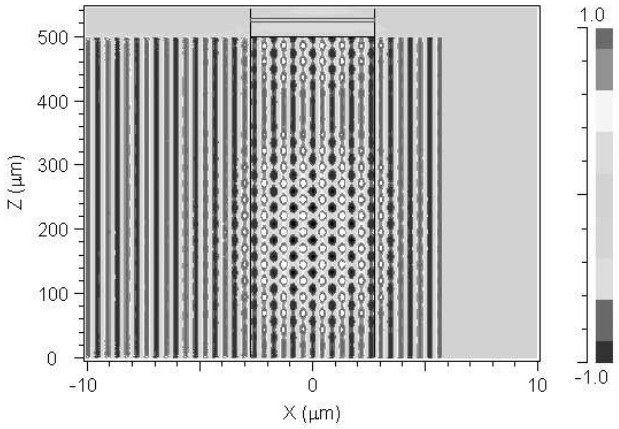


Figure 51: Electric field for grating input showing poor coupling efficiency.

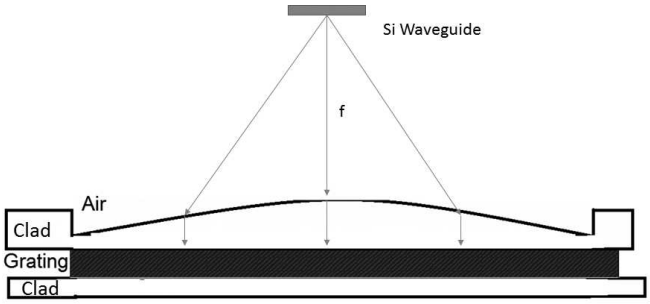


Figure 52: Lensed grating coupler setup.

The loss of the lensed grating coupler can be broken down to three factors: Losses from collimated light that does not couple in to the waveguide all the way; losses from skew rays, or rays that don't hit or reflect off the lens; and losses from non-collimation of the light into the grating. Each of these factors will be explored separately to describe the overall coupling efficiency of the grating.

### 6.5.1 Collimated Light Losses

All gratings are not perfectly efficient even if light hits the grating at only one angle loss can occur as a result of the grating itself, such as the grating vector, the length of the grating, and the core index contrast. Since the core index contrast of the Dow Corning material is fixed at 0.003, the

other parameters need to be optimized. Using an angled FDTD simulation, the optimal grating period is found. For this simulation, a grating of length 100 $\mu$m was modeled. The grating angle was set at 45° due to analysis done with the RCWA simulation at normal input coupling. Figure 53a shows the coupling tolerance of the straight waveguide. It shows that the optimal grating period is 0.6105 $\mu$m, which is close to the first order approximation of 0.615 $\mu$m. If the coupling efficiency is within $\pm 0.01$ $\mu$m the coupling efficiency varies by less than 5%.

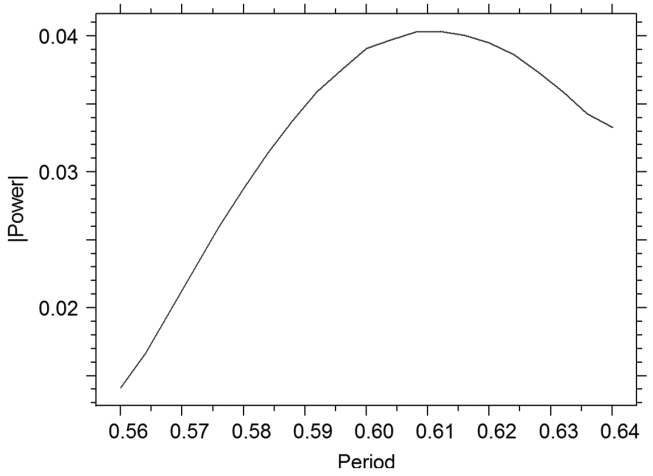


(a) FDTD optimal grating period, ($\Lambda$).

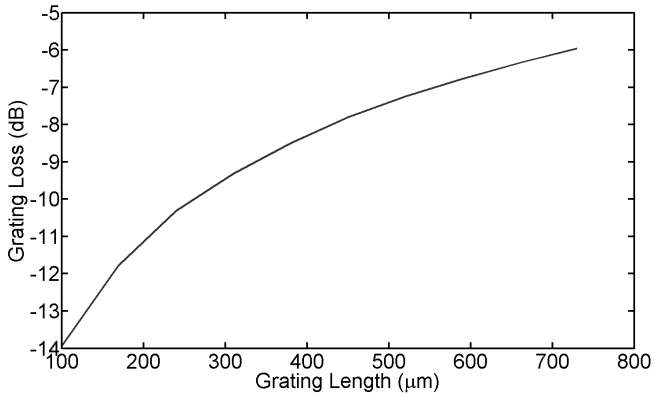


(b) FDTD length of grating efficiency.

Figure 53: FDTD collimated light losses.

Using the optimal grating period given in Figure 53a, another FDTD simulation was conducted varying the length of the waveguide. Figure 53b shows how the efficiency of the grating increases

as the length of the waveguide increases. The length simulation shows that for a grating length of 700 $\mu$m, the grating has a -6.0 dB coupling loss. The grating couplers are not very efficient and a long grating needs to be used. Unfortunately, to simulate a grating of this size would be very time consuming, a grating of 2 mm would take 9770 MB of memory and take 270 hours to complete for one simulation alone, and is not very practical. To save the time of simulating the grating up to 2 mm in length, coupling efficiency of a grating depending on the length was used [64]

$$CE = 1 - e^{\alpha L} \tag{98}$$

where $\alpha$ is the coupling coefficient and $L$ is the length of the grating. Solving for the coupling coefficient gives

$$\alpha = \frac{\log(1 - CE)}{L} \tag{99}$$

which is constant for every length of the waveguide, $L$. Figure 54 shows that the coupling coefficient, $\alpha$, is constant across the simulation within 3%, therefore the coupling efficiency can be estimated using Equation 99. The resulting interpolation is shown in Figure 55. This shows that if the grating length is 2 mm, the coupling loss is -2.6 dB.

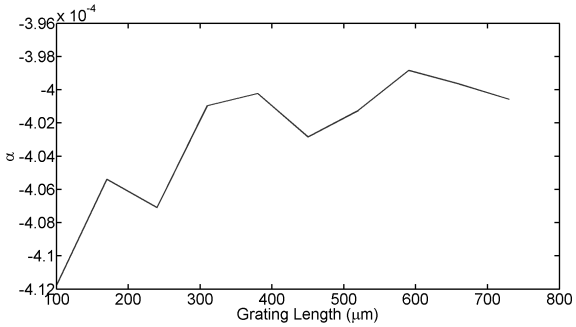


Figure 54: Coupling coefficient across length of the grating.

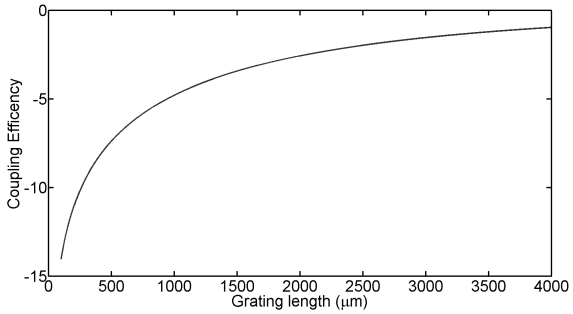


Figure 55: Interpolation to grating length efficiency.

### 6.5.2 Skew Ray Lossses

The next loss that needs to be calculated is the skew ray loss. This measures the amount of rays that do not hit the lens coupler. The output field of a silicon waveguide, shown in Figure 38, can be modeled as a uniform point source for distances more than 10 $\mu$m away from the end of the silicon waveguide. Using the geometry shown in Figure 56 to determine the skew loss, assuming the output is a point source, the skew loss can be written as

$$Loss = \frac{P_{lens}}{P_{radiates}} = \frac{\sin^{-1}\left(\frac{R}{f}\right)}{\pi} \tag{100}$$

Where $R$ is the radius of the lens, $f$ is the focal length of the lens. To a collimaing lens, the silicon waveguide needs to be placed on the focal length of the lens. Therefore, the focal length of the lens can be related to the radius of the lens by

$$\frac{1}{f} = (n-1)\left(\frac{1}{R_1} - \frac{1}{R_2} + \frac{(n-1)d}{nR_1R_2}\right) \tag{101}$$

Where $R_1$ is the radius of the surface closest to the source waveguide, $R_2$ is the radius of the farthest surface, and $d$ is the thickness of the lens. Since $R_2 = \infty$, the lens makers equation can be simplified to

$$R = f\,(n-1) \tag{102}$$

Simplifying the skew ray calculation to

$$Loss = \sin^{-1}(n-1). \tag{103}$$

This means that no matter the collimating lens is situated, a constant loss occurs. Using the Dow Corning cladding index as the lens index, a loss of -2.76 dB is experienced.

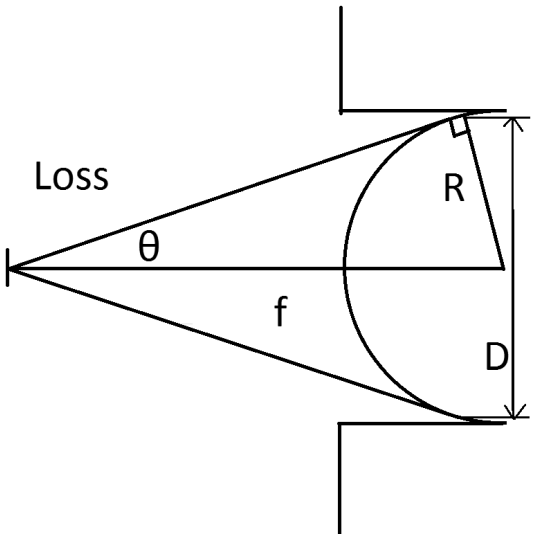


Figure 56: Geometry setup to determine skew ray loss.

This does not mean that the coupler should be positioned arbitrarily. The further the lens is from the end of the silicon waveguide the larger the lens radius is, therefore the larger the maximum grating length, $D$. The maximum grating length is

$$D = \frac{2\,R\,\sqrt{f^2 - R^2}}{f} \tag{104}$$

$$D = 2\,f\,(n-1)\,\sqrt{n(2-n)}. \tag{105}$$

### 6.5.3 Non-Collimation Losses

The final loss in the grating system is the loss that occurs when a wave hits a grating at a angle that isn't normal to the grating. The FDTD method was used to find the input coupling efficiency of input plane waves that are slightly off the normal optical axis. Grating lengths of 200 $\mu$m were simulated. The resulting coupling efficiency is shown in Figure 57.

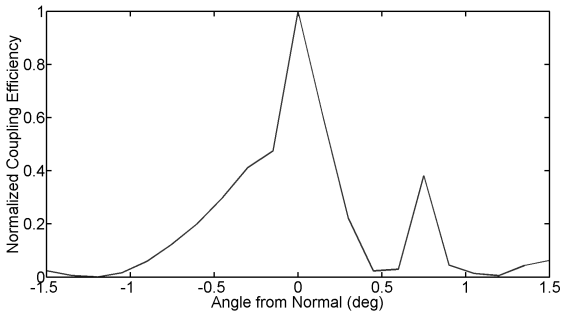


Figure 57: Coupling efficiency of off axis input plane waves.

Even if the lens is a perfect lens, diffraction effects keep the lens from perfectly collimating the incoming wave. In Section 6.5.1 it was determined that a grating of 2 mm was necessary for efficient coupling. Using Equation 105 it was found that the lens needed to be 1 mm from the silicon waveguide. Using these parameters the collimating lens was optimized in ZEMAX to minimize lens abberations. Because the lens will be micromolded, it is possible to impart any shape into the lens, therefore the optimization parameters included both the lens radius and the lens conic. This makes the molded lens an aspheric lens. The equation of the surface is given by

$$x(r) = \frac{r^2}{R(1+\sqrt{1-(1+\kappa)\frac{r^2}{R^2}})} \tag{106}$$

where $r$ is the distance from the axis and $\kappa$ is the conic constant.

The optimized parameters for coupling a collimating lens with a focal length of 1 mm and a lens to grating distance of 0.5 mm was found. The radius of curvature, $R$, of 0.506 mm and a conic constant, $\kappa$, of -2.267. The profile of the output waveform is shown in Figure 58.

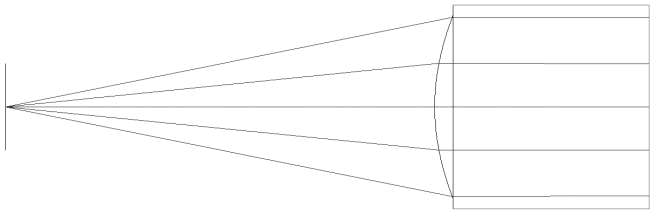

Figure 58: Collimating Lens.

Using ZEMAX the fast Fourier transform point spread function (FFT PSF) was found to determine the output angles. Figure 59a shows what the output relative intensity when the waveguide is centered on the optical axis. To attain alignment tolerances, the silicon waveguide was allowed to go off the optical axis of the lens. Figure 59b shows the relative output intensity when the silicon waveguide is 0.1 $\mu$m off the optical axis.

Applying the output intensity of the grating profiles to the off axis losses, the alignment tolerance was obtained, shown in Figure 60. Figure 60 shows that the coupling efficiency of the lens peaks at 0.814 when the lens is 40 $\mu$m off axis of the coupler. To get under 2 dB loss from the off axis loss, the coupler has an alignment tolerance of $\pm$40 $\mu$m. The interesting thing about the coupling efficiency is that it peaks again when the input beam is off center. This peak is due to the second peak in the off axis coupling efficiency in Figure 57.

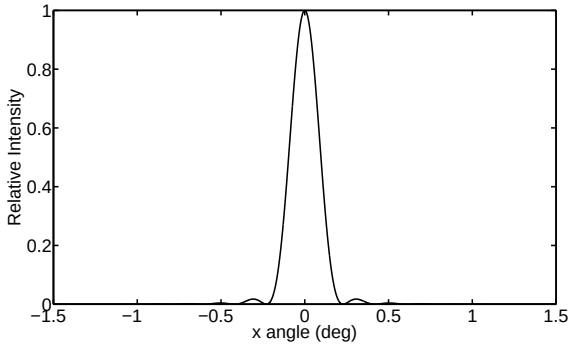


(a) Output point spread function for Si waveguide on axis with the lens.

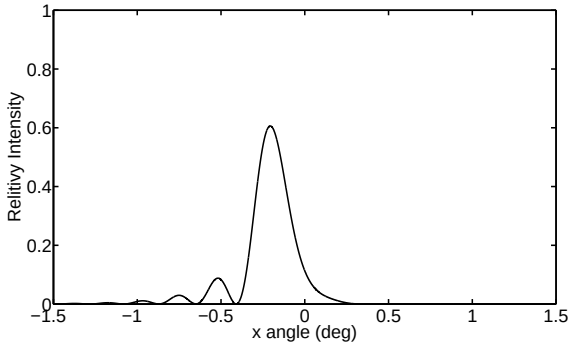


(b) Output point spread function for Si waveguide off axis by 0.1 $\mu$m.

Figure 59: ZEMAX FFT PSF profiles.

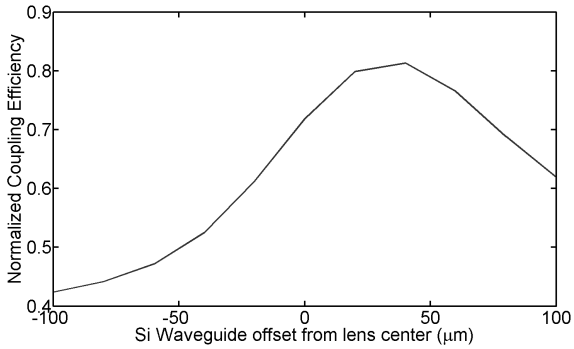


Figure 60: Alignment tolerance of grating coupler.

## 6.6 Conclusion

Two grating couplers to couple light from silicon waveguides to polymer single mode fibers were investigated for use in printed circuit boards. A focusing grating coupler, in which the grating

period and the grating angle changed along the direction of the grating length, was designed and evaluated. This coupler gave a coupling efficiency of -14 dB, of the light incident upon the coupler. This coupler was also deemed difficult to manufacture in a non laboratory setting. The second coupler consisted of a lensed grating where the grating angle and the grating period was constant throughout the entire waveguide. The grating period of this coupler was found to be 610.5 nm and the grating angle was found to be 45°. The length of the grating needed to be at least 2 mm for coupling losses greater than -2.6 dB. The grating also suffered from a constant loss of -2.76 dB due to skew ray losses. The grating alignment tolerances were also modeled. The highest efficiency is when the lens leads the grating by 40 $\mu$m this gives a loss of 0.90 dB. To stay within a 2 dB loss the lens and the silicon waveguide must be aligned by $\pm 40$ $\mu$m.

# References


[1] J. Hecht, *City of Light : The Story of Fiber Optics: The Story of Fiber Optics*, ser. Sloan Technology Series. Oxford University Press, USA, 1999. [Online]. Available: http://books.google.com/books?id=r7HqAvWGUUkC

[2] M. Jones and K. Kao, "Spectrophotometric studies of ultra low loss optical glasses ii: double beam method," *Journal of Physics E: Scientific Instruments*, vol. 2, no. 4, p. 331, 1969.

[3] D. STIGLIANI, "Light interface technology(optical communication technique based on fiber optic light pipes and time, space or wavelength division multiplexing)," in *International Electromagnetic Compatibility Symposium, Philadelphia, Pa*, 1971, pp. 316–321.

[4] L. B. Kish, "End of moore's law: thermal (noise) death of integration in micro and nano electronics," *Physics Letters A*, vol. 305, no. 3, pp. 144–149, 2002.

[5] J. Gambino, F. Chen, and J. He, "Copper interconnect technology for the 32 nm node and beyond," in *Custom Integrated Circuits Conference, 2009. CICC '09. IEEE*, sept. 2009, pp. 141 –148.

[6] H. Cho, P. Kapur, and K. C. Saraswat, "Power comparison between high-speed electrical and optical interconnects for interchip communication," *Journal of Lightwave Technology*, vol. 22, no. 9, p. 2021, 2004.

[7] D. Huang, T. Sze, A. Landin, R. Lytel, and H. Davidson, "Optical interconnects: out of the box forever?" *IEEE J. Sel. Top. Quant.*, vol. 9, no. 2, pp. 614 – 623, march-april 2003.

[8] C. Berger, M. A. Kossel, C. Menolfi, T. Morf, T. Toifl, and M. L. Schmatz, "High-density optical interconnects within large-scale systems," in *Photonics Fabrication Europe*. International Society for Optics and Photonics, 2003, pp. 222–235.

[9] N. Savage, "Linking with light [high-speed optical interconnects]," *IEEE Spectrum*, vol. 39, no. 8, pp. 32 – 36, aug 2002.

[10] A. Neyer, S. Kopetz, E. Rabe, W. Kang, and S. Tombrink, "Electrical-optical circuit board using polysiloxane optical waveguide layer," in *Electronic Components and Technology Conference, 2005. Proceedings. 55th*, 31 2005-june 3 2005, pp. 246 –250.

[11] J. Dingeldein, K. L. Kruse, C. Demars, C. Middlebrook, C. Friedrich, and M. Roggemann, "Optical-electrical printed wiring board for high-speed computing applications," *Optical Engineering*, vol. 52, no. 3, pp. 035 201–035 201, 2013. [Online]. Available: + http://dx.doi.org/10.1117/1.OE.52.3.035201

[12] T. Shiina, K. Shiraishi, and S. Kawakami, "Waveguide-bend configuration with low-loss characteristics," *Opt. Lett.*, vol. 11, no. 11, pp. 736–738, 1986.

[13] F. Yu and X. Yang, *Introduction to Optical Engineering*. Cambridge University Press, 1997. [Online]. Available: http://books.google.com/books?id=RYm7WwjsyzkC

[14] K. Yee, "Numerical solution of initial boundary value problems involving maxwell's equations in isotropic media," *Antennas and Propagation, IEEE Transactions on*, vol. 14, no. 3, pp. 302 –307, may 1966.

[15] M. D. Feit and J. J. A. Fleck, "Computation of mode properties in optical fiber waveguides by a propagating beam method," *Appl. Opt.*, vol. 19, no. 7, pp. 1154–1164, Apr 1980. [Online]. Available: http://ao.osa.org/abstract.cfm?URI=ao-19-7-1154

[16] W. Huang, C. Xu, S.-T. Chu, and S. Chaudhuri, "The finite-difference vector beam propagation method: analysis and assessment," *Lightwave Technology, Journal of*, vol. 10, no. 3, pp. 295 –305, mar 1992.

[17] D. G. Voelz and M. C. Roggemann, "Digital simulation of scalar optical diffraction: revisiting chirp function sampling criteria and consequences," *Appl. Opt.*, vol. 48, no. 32, pp. 6132–6142, Nov 2009. [Online]. Available: http://ao.osa.org/abstract.cfm?URI=ao-48-32-6132

[18] B. W. Swatowski, C. M. Amb, S. K. Breed, D. J. Deshazer, W. K. Weidner, R. F. Dangel, N. Meier, and B. J. Offrein, "Flexible, stable, and easily processable optical silicones for low loss polymer waveguides," in *Society of Photo-Optical Instrumentation Engineers*

*(SPIE) Conference Series*, ser. Society of Photo-Optical Instrumentation Engineers (SPIE) Conference Series, vol. 8622, Feb. 2013.

[19] P. P. Naulleau, "Relevance of mask-roughness-induced printed line-edge roughness in recent and future extreme-ultraviolet lithography tests," *Appl. Opt.*, vol. 43, no. 20, pp. 4025–4032, 2004.

[20] C.-Y. Chao and L. J. Guo, "Reduction of surface scattering loss in polymer microrings using thermal-reflow technique," *IEEE Photonic. Tech. L.*, vol. 16, no. 6, pp. 1498–1500, 2004.

[21] T. Ling, S.-L. Chen, and L. J. Guo, "Fabrication and characterization of high q polymer micro-ring resonator and its application as a sensitive ultrasonic detector," *Opt. Express*, vol. 19, no. 2, pp. 861–869, Jan 2011. [Online]. Available: http://www.opticsexpress.org/abstract.cfm?URI=oe-19-2-861

[22] B. G. Streetman and S. Banerjee, *Solid state electronic devices*. Prentice Hall New Jersey, 2000, vol. 4.

[23] A. Di Donato, M. Farina, D. Mencarelli, A. Lucesoli, S. Fabiani, T. Rozzi, G. M. Di Gregorio, and G. Angeloni, "Stationary mode distribution and sidewall roughness effects in overmoded optical waveguides," *Lightwave Technology, Journal of*, vol. 28, no. 10, pp. 1510–1520, 2010.

[24] E. Griese, "Modeling of highly multimode waveguides for time-domain simulation," *Selected Topics in Quantum Electronics, IEEE Journal of*, vol. 9, no. 2, pp. 433–442, 2003.

[25] D. Lenz, D. Erni, and W. Bchtold, "Modal power loss coefficients for highly overmoded rectangular dielectric waveguides based on free space modes," *Opt. Express*, vol. 12, no. 6, pp. 1150–1156, 2004.

[26] I. Papakonstantinou, R. James, and D. R. Selviah, "Radiation- and bound-mode propagation in rectangular, multimode dielectric, channel waveguides with sidewall roughness," *Lightwave Technology, Journal of*, vol. 27, no. 18, pp. 4151–4163, 2009.

[27] I. Papakonstantinou, K. Wang, D. R. Selviah, and F. A. Fernndez, "Transition, radiation and propagation loss in polymer multimode waveguide bends," *Opt. Express*, vol. 15, no. 2, pp. 669–679, 2007.

[28] L. Lewin, D. C. Chang, and E. F. Kuester, Eds., *Electromagnetic waves and curved structures*, vol. 2, 1977.

[29] K. R. Hiremath, M. Hammer, R. Stoffer, L. Prkna, and J. Čtyroký, "Analytical approach to dielectric optical bent slab waveguides," *Optical and Quantum Electronics*, vol. 37, no. 1-3, pp. 37–61, January 2005.

[30] Y. Okamura, S. Yoshinaka, and S. Yamamoto, "Measuring mode propagation losses of integrated optical waveguides: a simple method," *Appl. Opt.*, vol. 22, no. 23, pp. 3892–3894, 1983.

[31] D. Yevick, "A guide to electric field propagation techniques for guided-wave optics," *Optical and Quantum Electronics*, vol. 26, no. 3, pp. S185–S197, 1994.

[32] R. D. Grounp, *BeamPROP Maunal Revision C*, Rsoft Design Group, Inc, Ossinging, NY, 2011.

[33] D. Marcuse, *Theory of dielectric optical waveguides*, ser. Quantum electronics–principles and applications. Boston :: Academic Press, 1991.

[34] T. S. H. Nishihara, M. Haruna, *Optical integrated circuits*, ser. McGraw-Hill optical and electro-optical engineering series. New York: McGraw-Hill Book Co., 1989.

[35] G. B. Hocker and W. K. Burns, "Mode dispersion in diffused channel waveguides by the effective index method," *Appl. Opt.*, vol. 16, no. 1, pp. 113–118, Jan 1977. [Online]. Available: http://ao.osa.org/abstract.cfm?URI=ao-16-1-113

[36] *MicroXAM Manual.*

[37] X. Wang, W. Jiang, L. Wang, H. Bi, and R. T. Chen, "Fully embedded board-level optical interconnects from waveguide fabrication to device integration," *J. Lightwave Technol.*, vol. 26, no. 2, pp. 243–250, 2008.

[38] M. Heiblum and J. Harris, "Analysis of curved optical waveguides by conformal transformation," *IEEE J. Quantum Elect.*, vol. 11, no. 2, pp. 75–83, 1975.

[39] L. Robitaille, C. L. Callender, and J. P. Noad, "Polymer waveguide devices for wdm applications," pp. 14–24, 1998. [Online]. Available: + http://dx.doi.org/10.1117/12.305417

[40] L. B. Aronson, B. E. Lemoff, L. A. Buckman, and D. W. Dolfi, "Low-cost multimode wdm for local area networks up to 10 gb/s," *Photonics Technology Letters, IEEE*, vol. 10, no. 10, pp. 1489–1491, 1998.

[41] A. Melloni, R. Costa, P. Monguzzi, and M. Martinelli, "Ring-resonator filters in silicon oxynitride technology for dense wavelength-division multiplexing systems," *Optics letters*, vol. 28, no. 17, pp. 1567–1569, 2003.

[42] E. A. Marcatili, "Dielectric rectangular waveguide and directional coupler for integrated optics," *Bell Syst. Tech. J*, vol. 48, no. 7, pp. 2071–2102, 1969.

[43] T. Kitoh, N. Takato, M. Yasu, and M. Kawachi, "Bending loss reduction in silica-based waveguides by using lateral offsets," *Lightwave Technology, Journal of*, vol. 13, no. 4, pp. 555–562, 1995.

[44] E. Hecht, *Optics*. Addison-Wesley Longman, Incorporated, 2002. [Online]. Available: http://books.google.com/books?id=7aG6QgAACAAJ

[45] L. B. Soldano and E. C. M. Pennings, "Optical multi-mode interference devices based on self-imaging: principles and applications," *Lightwave Technology, Journal of*, vol. 13, no. 4, pp. 615–627, 1995.

[46] J. W. Goodman, *Introduction to Fourier Optics*, 3rd ed. Roberts & Company Publishers, Dec. 2004.

[47] B. W. Swatowski, C. T. Middlebrook, K. Walczak, and M. C. Roggemann, "Optical loss characterization of polymer waveguides on halogen and halogen-free fr-4 substrates," in *Proceedings of SPIE*, vol. 7944, 2011, p. 794409.

[48] L. Thyln, "The beam propagation method: an analysis of its applicability," *Opt. Quant. Electron.*, vol. 15, pp. 433–439, 1983.

[49] S. Odate, C. Koike, H. Toba, T. Koike, A. Sugaya, K. Sugisaki, K. Otaki, and K. Uchikawa, "Angular spectrum calculations for arbitrary focal length with a scaled convolution," *Opt. Express*, vol. 19, no. 15, pp. 14 268–14 276, Jul 2011.

[50] N. Lindlein, "Simulation of micro-optical systems including microlens arrays," *Journal of Optics A: Pure and Applied Optics*, vol. 4, no. 4, p. S1, 2002. [Online]. Available: http://stacks.iop.org/1464-4258/4/i=4/a=351

[51] M. Bass, C. DeCusatis, J. Enoch, V. Lakshminarayanan, G. Li, C. MacDonald, V. Mahajan, and E. Van Stryland, *Handbook of Optics, Third Edition Volume IV: Optical Properties of Materials, Nonlinear Optics, Quantum Optics (set)*, ser. Handbook of Optics. Mcgraw-hill, 2009. [Online]. Available: http://books.google.com/books?id=1CES2tOBwikC

[52] G. Ghosh, "Dispersion-equation coefficients for the refractive index and birefringence of calcite and quartz crystals," *Optics Communications*, vol. 163, no. 13, pp. 95 – 102, 1999. [Online]. Available: http://www.sciencedirect.com/science/article/pii/S0030401899000917

[53] M. Li and S. J. Sheard, "Experimental study of waveguide grating couplers with parallelogramic tooth profiles," *Optical Engineering*, vol. 35, no. 11, pp. 3101–3106, 1996. [Online]. Available: + http://dx.doi.org/10.1117/1.601047

[54] M. Veith, K. Müller, S. Mittler-Neher, and W. Knoll, "Propagation and deflection of guided modes in planar waveguides via grating rotation," *Applied Physics B*, vol. 60, no. 1, pp. 1–4, 1995.

[55] M. Moharam, E. B. Grann, D. A. Pommet, and T. Gaylord, "Formulation for stable and efficient implementation of the rigorous coupled-wave analysis of binary gratings," *JOSA A*, vol. 12, no. 5, pp. 1068–1076, 1995.

[56] M. Moharam and T. Gaylord, "Rigorous coupled-wave analysis of planar-grating diffraction," *JOSA*, vol. 71, no. 7, pp. 811–818, 1981.

[57] W. Driemeier, "Coupled-wave analysis of the bragg effect waveguide coupler," *Journal of modern optics*, vol. 38, no. 2, pp. 363–377, 1991.

[58] N. van der Aa, "Diffraction grating theory with rcwa or the c method," in *Progress in Industrial Mathematics at ECMI 2004*. Springer, 2006, pp. 99–103.

[59] S. M. Schultz, E. N. Glytsis, and T. K. Gaylord, "Design of a high-efficiency volume grating coupler for line focusing," *Appl. Opt.*, vol. 37, no. 12, pp. 2278–2287, Apr 1998. [Online]. Available: http://ao.osa.org/abstract.cfm?URI=ao-37-12-2278

[60] J. R. Lawrence, G. A. Turnbull, and I. D. Samuel, "Polymer laser fabricated by a simple micromolding process," *Applied physics letters*, vol. 82, no. 23, pp. 4023–4025, 2003.

[61] T. Aoyagi, Y. Aoyagi, and S. Namba, "High-efficiency blazed grating couplers," *Applied Physics Letters*, vol. 29, p. 303, 1976.

[62] W. Driemeier, "Bragg-effect grating couplers integrated in multicomponent polymeric waveguides," *Optics letters*, vol. 15, no. 13, pp. 725–727, 1990.

[63] K. O. Hill and G. Meltz, "Fiber bragg grating technology fundamentals and overview," *Lightwave Technology, Journal of*, vol. 15, no. 8, pp. 1263–1276, 1997.

[64] S.-D. Wu and E. N. Glytsis, "Volume holographic grating couplers: rigorous analysis by use of the finite-difference frequency-domain method," *Appl. Opt.*, vol. 43, no. 5, pp. 1009–1023, Feb 2004. [Online]. Available: http://ao.osa.org/abstract.cfm?URI=ao-43-5-1009